



BACHELORTHESIS

Quantum Phase Transitions and Dynamics in Strongly Correlated Systems: An Infinite Matrix Product State Approach

vorgelegt von

Pascal Sievers

am 24.06.2025

MIN-Fakultät, Fachbereich Informatik

Deutsches Zentrum für Luft- und Raumfahrt, (Institut für Softwaretechnologie, Abteilung High Performance Computing)

Studiengang: Computing in Science, SP Physik

Matrikelnummer: 7504482

Erstgutachter: PD Dr. Satoshi Ejima Zweitgutachter: Prof. Dr. Dieter Jaksch

Abstract

This thesis explores non-equilibrium phenomena in strongly correlated quantum systems, focusing on the half-filled one-dimensional Hubbard model at zero temperature in the thermodynamic limit. Using tensor network methods, particularly infinite matrix product states (iMPS), we simulate the real-time dynamics induced by optical pump pulses. A laser pulse is modeled by a time-dependent vector potential applied via the Peierls substitution, with dynamics computed using the infinite time-evolving block decimation (iTEBD) algorithm. We investigate the emergence of a superconducting-like η -pairing state with off-diagonal long-range order (ODLRO) and confirm that η -pairing correlations are significantly enhanced for certain pulse parameters. Additionally, signatures of dynamical quantum phase transitions (DQPTs) are observed in the Loschmidt echo rate function. Finite-entanglement scaling is employed to extract the central charge and analyze criticality of the ground state.

Zusammenfassung

In dieser Arbeit werden Nichtgleichgewichtsphänomene in stark korrelierten Quantensystemen untersucht, mit Schwerpunkt auf dem halbgefüllten eindimensionalen Hubbard-Modell bei T=0 im thermodynamischen Limes. Mithilfe von Tensornetzwerk-Methoden, insbesondere unendlichen Matrixproduktzuständen (iMPS), simulieren wir die Echtzeitdynamik, die durch Laserpulse ausgelöst wird. Ein Laserpuls wird durch ein zeitabhängiges Vektorpotential modelliert, das über die Peierls-Substitution angewendet wird, wobei die Zeitentwicklung mit dem iTEBD Algorithmus berechnet wird. Wir untersuchen das Auftreten eines supraleitungsähnlichen η -Paar-Zustands mit nicht-diagonaler langreichweitiger Ordnung (ODLRO) und bestätigen, dass die η -Paarungskorrelationen für bestimmte Pulsparameter signifikant verstärkt werden. Außerdem werden Anzeichen dynamischer Quantenphasenübergänge (DQPTs) in der Ratenfunktion des Loschmidt-Echos beobachtet. Es wird finite-entanglement scaling eingesetzt, um die Zentralladung des Grundzustands zu berechnen.

Contents

Abstract		
1.	Introduction	1
2.	Theoretical Backround 2.1. Many-Particle Systems 2.1.1. First Quantization 2.1.2. Second Quantization 2.1.3. Operators in Second Quantization 2.1.4. Hubbard Model 2.1.5. Half-Filled Hubbard Chain 2.1.6. Pairing and Off-Diagonal Long-Range Order 2.1. Entropy of Entanglement 2.1. Dynamics and Non-Equilibrium 2.1. Photoinduced Hubbard Model 2.1. Quantum Quenches 2.1. Dynamical Quantum Phase Transitions	2 2 2 3 4 4 5 6 7 9 10 12 12
3.	Numerical Methods 3.1. Tensor Networks 3.1.1. Matrix Product States 3.1.2. Infinite Matrix Product States 3.2. Algorithms 3.2.1 iTEBD 3.2.2 VUMPS 3.2.3. Jordan-Wigner Transformation 3.3. Finite-Entanglement Scaling	15 15 17 20 20 21 22 22
4.		24 24 26 27 27 31 35
5.	Conclusion and Outlook	41
Α.	Additional Data	42
Bibliography		44
Acknowledgements		51

1. Introduction

In recent years, the study of non-equilibrium dynamics in quantum many-body systems has become an active area of research [1, 2] in condensed matter physics and quantum information. Exploring systems far from equilibrium promises access to new and interesting phenomena beyond the constraints of equilibrium statistical physics. Experimental advances [1, 3–6], particularly in cold atoms in optical lattices and trapped ions, have made it possible to probe strongly correlated systems under non-equilibrium conditions and call for a better theoretical understanding of how complex quantum systems evolve over time.

Alongside analytical theory and experiment, numerical simulations have become an essential third pillar in understanding strongly correlated quantum many-body systems. Yet the exponential growth of the Hilbert space with system size quickly renders many numerical approaches, such as exact diagonalization, intractable even for modestly sized systems. To address this challenge, tensor network techniques [7, 8] exploit the typically low entanglement of ground and low-lying excited states, enabling an efficient encoding of one-dimensional quantum many-body systems. In this thesis, we use the infinite matrix product state (iMPS) formalism [9, 10] to simulate quantum dynamics directly in the thermodynamic limit, i.e., for infinite systems, avoiding finite-size effects. We use an existing implementation of the variational uniform matrix product state (VUMPS) ground state search algorithm [11], alongside custom implementations for real-time evolution using the infinite time-evolving block decimation (iTEBD) algorithm [9], as well as for the computation of relevant observables.

A paradigmatic model to describe a system of strongly correlated electrons is the one-dimensional Hubbard model [12], which captures the essential competition between kinetic energy and on-site Coulomb repulsion. Despite its apparent simplicity, the model exhibits a rich variety of phenomena and, crucially, is analytically integrable. This makes it an ideal benchmark for numerical approaches and an excellent framework for studying quantum dynamics. At half-filling and zero temperature, the model describes a Mott insulator with a gapless spin sector and power-law decaying spin correlations, providing a setting to study quantum criticality. In addition, the Hubbard model possesses an η -pairing symmetry, which is central to the study of unconventional superconducting states.

The primary focus of this thesis is the real-time dynamics of the half-filled one-dimensional Hubbard model under time-dependent external driving, specifically in the form of optical pump pulses. We are particularly interested in the possibility of dynamically inducing unconventional superconducting-like states, containing so-called η -pairs [13–16], which exhibit off-diagonal long-range order (ODLRO) [17] and provide a conceptual framework for understanding non-equilibrium superconductivity.

We also explore the occurrence of dynamical quantum phase transitions (DQPTs) [18, 19], which generalize the concept of quantum phase transitions to the time domain. These transitions manifest as non-analyticities in the Loschmidt echo, a measure of the return probability to the initial state, and offer an interesting perspective on the dynamics in quantum many-body systems beyond equilibrium. To characterize the nature of the system after photoexcitation, we also use finite-entanglement scaling [20, 21] to gain insight into criticality and the possibility of extracting a central charge.

Thesis outline. Chapter 2 presents the theoretical background, including second quantization, the Hubbard model and its η -pairing symmetry, as well as the concept of DQPTs. Chapter 3 introduces the numerical methods used, focusing on tensor networks, iMPS, and the iTEBD algorithm. Chapter 4 discusses the main results, including correlation functions, entanglement, and post-pulse dynamics. Finally, Chapter 5 summarizes the findings and outlines possible directions for future research.

Theoretical Backround

2.1. Many-Particle Systems

In this section, we give an overview of the formalism of quantum-many-body systems by introducing the notion of second quantization. The introduction is based on Ref. [22, Chapter XIV] and Ref. [23, Chapter XV].

2.1.1. First Quantization

We start with the well known single-particle quantum mechanics. The state of a system is given by a wavefunction $|\psi\rangle$, which lies in the Hilbert space \mathcal{H}_1 . This state space is spanned by a complete set of eigenfunctions $\{|u_i\rangle\}$ generated by a complete set of commuting observables.

To describe multiple identical particles, we set up a new state space as the tensor product

$$\mathcal{H}_N = \mathcal{H}_1^{(1)} \otimes \mathcal{H}_1^{(2)} \otimes \cdots \otimes \mathcal{H}_1^{(N)}$$
(2.1)

of single-particle state spaces $\mathcal{H}_1^{(j)}$. The index (j) indicates that the identical particles are, at this stage, still mathematically distinguishable. A basis of \mathcal{H}_N can be constructed from the single-particle bases $\{|u_{i_j}^{(j)}\rangle\}$ of $\mathcal{H}_1^{(j)}$:

$$\left\{ |u_{i_1}^{(1)}\rangle \otimes |u_{i_2}^{(2)}\rangle \otimes \cdots \otimes |u_{i_N}^{(N)}\rangle | i_1, \dots i_N = 1, \dots, \dim \mathcal{H}_1 \right\}. \tag{2.2}$$

Any single-particle operator $\hat{O}_1^{(j)}$ can also be extended to \mathcal{H}_N as

$$\mathbb{1}_{\mathcal{H}_1}^{(1)} \otimes \cdots \otimes \hat{O}_1^{(j)} \otimes \cdots \otimes \mathbb{1}_{\mathcal{H}_1}^{(N)}, \tag{2.3}$$

where $\mathbb{1}_{\mathcal{H}_1}^{(j)}$ is the identity operator on $\mathcal{H}_1^{(j)}$. With that we can now represent any state vector in \mathcal{H}_N using the basis (2.2) and any operator on \mathcal{H}_N as a linear combination of (2.3).

For a correct description, we must also take into account that identical quantum-mechanical particles are indistinguishable. Since the physical state does not change (i.e. there is no measurement that can distinguish) when two identical particles of a multi-particle state are exchanged, we currently have several basis vectors that all correspond to the same physical state. Furthermore, it can be shown (see example A-3-b in Ref. [22, Chapter XIV]) that the choice of the specific basis vector can incorrectly affect the probability of measurements, which should not be the case. In order to resolve this so-called exchange degeneracy, we map all linearly independent vectors that represent the same physical state to one distinct vector. This can be done in two different ways using the two different projectors

$$\hat{S}_N = \frac{1}{N!} \sum_{\sigma \in S_N} \hat{P}_{\sigma}, \qquad \hat{A}_N = \frac{1}{N!} \sum_{\sigma \in S_N} \operatorname{sgn}(\sigma) \hat{P}_{\sigma}, \tag{2.4}$$

which project onto $\mathcal{H}_S(N)$ and $\mathcal{H}_A(N)$, respectively. \hat{P}_{σ} is a permutation operator and the sum runs over all permutations σ of the first N natural numbers.

Because $\mathcal{H}_S(N)$ and $\mathcal{H}_A(N)$ are orthogonal but for N > 2 not complementary subspaces of \mathcal{H}_N , we have restricted the state space for systems of identical particles and obtained two kinds of states. Physical states lie either in $\mathcal{H}_S(N)$ and are totally symmetric or in $\mathcal{H}_A(N)$ and are totally anti-symmetric with respect to particle exchange. In the case of totally symmetric states, the particles are called bosons. In the case of totally anti-symmetric states, the particles are called fermions.

2.1.2. Second Quantization

Using the introduced formalism for systems with more than just a few particles quickly gets very complicated due to the (anti-)symmetrization of wavefunctions (and operators). To simplify the notation and calculations, we will use the formalism of second quantization, which refers to an alternative method of labelling the states by eliminating the unphysical numbering of particles. It also introduces creation and annihilation operators, which change the particle number and thus act on a larger state space.

Occupation Number Representation

Since the particles are indistinguishable, we cannot assign a specific single-particle state to a specific particle, and it therefore makes no sense to number the particles. Instead, all the physical states contained in $\mathcal{H}_{A/S}(N)$ are uniquely characterized by the occupation numbers $\{n_1, n_2, \ldots, n_{\dim \mathcal{H}_1}\}$ where n_i is the occupation of the single-particle eigenstate $|u_i\rangle$ and $\sum_i n_i = N$. For fermions, n_i is either one or zero because \hat{A}_N applied to a state containing two or more particles in the same single-particle state yields zero (Pauli exclusion principle). A fermionic basis state can therefore be written as

$$|\underbrace{u_i, u_k, \dots, u_l, \dots}\rangle = \sqrt{N!} \, \hat{A}_N \, |u_i^{(1)}\rangle \otimes |u_k^{(2)}\rangle \otimes \dots \otimes |u_l^{(j)}\rangle \otimes \dots$$
 (2.5)

From the definition of \hat{A}_N (2.4), it follows that the sign of $|u_i, u_k, \ldots, u_l, \ldots\rangle$ changes when two particles are exchanged. Since any measurement only depends on the absolute value, the physical meaning does not change.

The following summary of second quantization will focus on fermionic systems, because these are the ones relevant to this work. For bosonic systems, please refer to Ref. [23, Chapter XV].

Fock Space

Dropping the constraint $\sum_{i} n_i = N$ generalizes the description of many-particle states and results in the extended Hilbert space

$$\mathcal{F} = \bigoplus_{N=0}^{\infty} \mathcal{H}_A(N), \tag{2.6}$$

called Fock space. Notice that the direct sum includes a state space with N=0 particles. The space $\mathcal{H}_A(0)$ is defined to be one-dimensional and consists of a single state, denoted as $|0\rangle$, which is referred to as the vacuum.

Creation and Annihilation Operators

In this bigger space, we now define the creation operator \hat{c}_i^{\dagger} and its hermitian conjugate, the annihilation operator \hat{c}_i . As the name suggests, the creation operator creates a new particle

$$\hat{c}_i^{\dagger} | u_k, \dots, u_l, \dots \rangle = | u_i, u_k, \dots, u_l, \dots \rangle \tag{2.7}$$

and the annihilation operator annihilates a particle

$$\hat{c}_i |u_i, u_k, \dots, u_l, \dots\rangle = |u_k, \dots, u_l, \dots\rangle.$$
(2.8)

Applying \hat{c}_i^{\dagger} to a state in which $|u_i\rangle$ is already occupied (i.e. $n_i = 1$) gives zero. The same is true for the application of \hat{c}_i to a state with $n_i = 0$. This behaviour enforces the Pauli exclusion principle.

From these definitions and the fact that $|u_i, u_k, \dots, u_l, \dots\rangle = -|u_k, u_i, \dots, u_l, \dots\rangle$, we can deduce the relations

$$\{\hat{c}_i, \hat{c}_j\} = \{\hat{c}_i^{\dagger}, \hat{c}_j^{\dagger}\} = 0, \quad \{\hat{c}_i, \hat{c}_j^{\dagger}\} = \delta_{ij}$$
 (2.9)

with the anticommutator $\{\hat{A}, \hat{B}\} = \hat{A}\hat{B} + \hat{B}\hat{A}$.

The occupation number operator $\hat{n}_i = \hat{c}_i^{\dagger} \hat{c}_i$ whose eigenvalue is n_i can also be defined.

2.1.3. Operators in Second Quantization

The complex (anti-)symmetrization of the first quantization has now been greatly simplified with the help of a new notation (2.5) and the commutation relations (2.9). However, to fully leverage the advantages of second quantization, operators should also have a simple representation in terms of creation and annihilation operators. Otherwise the new formalism would not be very useful.

There are two types of operators that need to be 'second-quantized': Single-particle operators such as the kinetic energy

$$\hat{T} = \sum_{i=1}^{N} \hat{t}(\hat{\mathbf{p}}_i) = \sum_{i=1}^{N} \frac{\hat{\mathbf{p}}_i^2}{2m}$$
(2.10)

and two-particle operators such as the coulomb interaction

$$\hat{U} = \sum_{i < j} \hat{u}(\hat{\mathbf{r}}_i, \hat{\mathbf{r}}_j) = \frac{1}{4\pi\varepsilon_0} \sum_{i < j} \frac{e^2}{|\hat{\mathbf{r}}_i - \hat{\mathbf{r}}_j|}.$$
 (2.11)

Single-Particle Operators

Using a single-particle orthonormal bases $\{|u_{i_j}^{(j)}\rangle\}$ of $\mathcal{H}_1^{(j)}$, it is easy to see that

$$\sum_{i=1}^{N} |u_{\alpha}^{(i)}\rangle\langle u_{\beta}^{(i)}| = \hat{c}_{\alpha}^{\dagger}\hat{c}_{\beta}. \tag{2.12}$$

Expanding \hat{T} with the completeness relation then leads to representation through creation and annihilation operators:

$$\hat{T} = \sum_{i=1}^{N} \hat{t}(\hat{\mathbf{p}}_{i}) = \sum_{i=1}^{N} \sum_{\alpha=1}^{\dim \mathcal{H}_{1}} |u_{\alpha}^{(i)}\rangle\langle u_{\alpha}^{(i)}| \,\hat{t}(\hat{\mathbf{p}}_{i}) \sum_{\beta=1}^{\dim \mathcal{H}_{1}} |u_{\beta}^{(i)}\rangle\langle u_{\beta}^{(i)}|
= \sum_{\alpha,\beta=1}^{\dim \mathcal{H}_{1}} \langle u_{\alpha}|\hat{t}(\hat{\mathbf{p}})|u_{\beta}\rangle \sum_{i=1}^{N} |u_{\alpha}^{(i)}\rangle\langle u_{\beta}^{(i)}|
= \sum_{\alpha,\beta=1}^{\dim \mathcal{H}_{1}} t_{\alpha,\beta} \,\hat{c}_{\alpha}^{\dagger} \hat{c}_{\beta},$$
(2.13)

with $t_{\alpha,\beta} = \langle u_{\alpha} | \hat{t}(\hat{\mathbf{p}}) | u_{\beta} \rangle$.

Two-Particle Operators

The same principle can be applied to two-particle operators, resulting in

$$\hat{U} = \frac{1}{2} \sum_{\alpha,\beta,\gamma,\delta}^{\dim \mathcal{H}_1} u_{\alpha,\beta,\gamma,\delta} \, \hat{c}_{\alpha}^{\dagger} \hat{c}_{\beta}^{\dagger} \hat{c}_{\gamma} \hat{c}_{\delta}, \tag{2.14}$$

2.2. Hubbard Model 5

with $u_{\alpha,\beta,\gamma,\delta} = \langle u'_{\alpha} | \langle u_{\beta} | \hat{u}(\hat{\mathbf{r}},\hat{\mathbf{r}}') | u_{\gamma} \rangle | u'_{\delta} \rangle$ and the factor $\frac{1}{2}$ to correct the double counting.

In this way, every operator can be expressed as a linear combination of products of creation and annihilation operators with matrix elements as coefficients. Thus, in general, the application of any operator—whether single-particle or two-particle—ultimately reduces to successive applications of creation and annihilation operators.

2.2. Hubbard Model

The Hubbard model is a fundamental model for interacting electrons in a lattice. It captures the essential competition between kinetic energy and onsite Coulomb repulsion, and has been widely studied as a minimal model for strong correlation effects. In this thesis, we focus on the properties of the one-dimensional, half-filled Hubbard model at zero temperature (T=0). The following introduction to the model is based on Refs. [12, Chapter 1] and [24, Chapter 6].

To analyze the interaction of electrons in a solid, we begin by making two simplifying approximations. First, we only consider the outer (valence/conduction) band and treat the inner electrons as part of a rigid ion core. This is justified if the Fermi surface lies inside or close to the conduction band and all other bands are far away. Second, the Born-Oppenheimer approximation can be used. Due to their much greater mass compared to the electrons, the ions can be viewed as stationary, resulting in a static lattice with up to two electrons per site $(|\uparrow\downarrow\rangle)$.

The general Hamiltonian for N electrons using these two approximations reads

$$\hat{H}' = \sum_{i=1}^{N} \left(\frac{\hat{\mathbf{p}}_i^2}{2m} + V_I(\hat{\mathbf{r}}_i) \right) + \sum_{i < j} V_C(\hat{\mathbf{r}}_i - \hat{\mathbf{r}}_j) = \sum_{i=1}^{N} \hat{t}(\hat{\mathbf{r}}_i, \hat{\mathbf{p}}_i) + \sum_{i < j} \hat{u}(\hat{\mathbf{r}}_i, \hat{\mathbf{r}}_j), \tag{2.15}$$

with the periodic potential of the ions $V_I(\hat{\mathbf{r}})$ and the Coulomb repulsion $V_C(\hat{\mathbf{r}}_i - \hat{\mathbf{r}}_j)$ between the electrons.

Using the rules (2.13) and (2.14) from the previous section, the Hamiltonian can now be mapped from first to second quantization:

$$\hat{H}' = \sum_{\alpha,\beta=1}^{\dim \mathcal{H}_1} t_{\alpha,\beta} \, \hat{c}_{\alpha}^{\dagger} \hat{c}_{\beta} + \frac{1}{2} \sum_{\alpha,\beta,\gamma,\delta}^{\dim \mathcal{H}_1} u_{\alpha,\beta,\gamma,\delta} \, \hat{c}_{\alpha}^{\dagger} \hat{c}_{\beta}^{\dagger} \hat{c}_{\gamma} \hat{c}_{\delta} \,. \tag{2.16}$$

Since electrons have a two-valued spin as an intrinsic property, the one-particle Hilbert spaces are composed of two parts: $\mathcal{H}_1 = \mathcal{H}_1^{\text{Angular}} \otimes \mathcal{H}_1^{\text{Spin}}$. The quantum numbers $\alpha, \beta, \gamma, \delta$ are therefore made up of spin σ and lattice site indices i, j, \ldots , where, for simplicity, we set the lattice spacing to one. The Hubbard model is obtained if only the most important matrix elements are taken into account. Screening shortens the Coulomb interaction range, so we consider only the diagonal elements representing the large on-site (intra-atomic) repulsion, neglecting weaker inter-atomic terms. This is believed to be a good approximation for transition and rare earth metals. For the first term in (2.16), we use the tight-binding approximation by only considering nearest-neighbour $\langle i, j \rangle$ matrix elements. The diagonal elements $t_{\alpha,\alpha}$ are set to zero, as they only add a constant energy-shift. In one dimension, this leaves us with the (one-band) Hubbard Hamiltonian:

$$\hat{H}'' = -t_h \sum_{\langle i,j \rangle, \sigma} \hat{c}_{i,\sigma}^{\dagger} \hat{c}_{j,\sigma} + \frac{U}{2} \sum_{j,\sigma,\sigma'} \hat{c}_{j,\sigma}^{\dagger} \hat{c}_{j,\sigma'}^{\dagger} \hat{c}_{j,\sigma'} \hat{c}_{j,\sigma}$$

$$= -t_h \sum_{j,\sigma} \left(\hat{c}_{j,\sigma}^{\dagger} \hat{c}_{j+1,\sigma} + \hat{c}_{j+1,\sigma}^{\dagger} \hat{c}_{j,\sigma} \right) + U \sum_{j} \underbrace{\hat{c}_{j,\uparrow}^{\dagger} \hat{c}_{j,\uparrow}}_{\hat{n}_{j,\uparrow}} \hat{c}_{j,\downarrow}^{\dagger} \hat{c}_{j,\downarrow}. \tag{2.17}$$

The hopping amplitude t_h determines the delocalization of electrons by lowering the kinetic energy if an electron is able to hop to a neighbouring site. The on-site Coulomb repulsion U increases the energy for every pair of electrons located at the same site.

Using an explicit basis, such as the Wannier functions, and employing density functional theory, the matrix elements can also be calculated. However, since the Hubbard model is the simplest description for an interacting electronic system, it is primarily used for the qualitative description of certain phenomena. Despite its simplicity, the model exhibits many interesting behaviours such as metallic conductivity, insulating states, a metal-insulator transition, antiferromagnetism, and more.

There are, however, real materials [25, 26] that are described by 'Hubbard-like' Hamiltonians, such as the multiband and extended Hubbard models as well as ongoing research to discover materials described by the one-band Hubbard model [27].

Hamiltonian at Half-Filling

Since the Hamiltonian (2.17) contains creation and annihilation operators only as pairs, the number of spin up- and down electrons is conserved. We can therefore add the term $-\frac{U}{2}\sum_{j}(\hat{n}_{j,\uparrow}+\hat{n}_{j,\downarrow})+\frac{U}{4}L$ with the number of lattice sites L to the Hamiltonian (2.17) without changing its eigenfunctions:

$$\hat{H} = \hat{H}'' - \frac{U}{2} \sum_{j} (\hat{n}_{j,\uparrow} + \hat{n}_{j,\downarrow}) + \frac{U}{4} L$$

$$= -t_h \sum_{j,\sigma} \left(\hat{c}_{j,\sigma}^{\dagger} \hat{c}_{j+1,\sigma} + \hat{c}_{j+1,\sigma}^{\dagger} \hat{c}_{j,\sigma} \right) + U \sum_{j} \left(\hat{n}_{j,\uparrow} - \frac{1}{2} \right) \left(\hat{n}_{j,\downarrow} - \frac{1}{2} \right)$$

$$= \hat{H}_{t_h} + \hat{H}_U.$$

$$(2.18)$$

In a canonical ensemble (constant N), this is simply a constant energy shift. In a grand canonical ensemble, this corresponds to introducing a chemical potential $\mu = U/2$ (plus a constant term), which leads to half-filling (N = L) [28, Chapter 8.7.1]. This formulation is also useful because of its higher symmetry than (2.17). For example, the Hamiltonian is now particle-hole symmetric, which means that it doesn't change under the transformation

$$\hat{c}_{j,\sigma} \to (-1)^j c_{j,\sigma}^{\dagger}. \tag{2.19}$$

2.2.1. Half-Filled Hubbard Chain

From now on, we focus on the half-filled case (2.18), where, on average, each lattice site is occupied by one electron, i.e., $\langle n \rangle = 1$. We also assume U > 0 to model a repulsive Coulomb potential. At half-filling, it is physically intuitive that for sufficiently large U, each lattice site hosts exactly one electron, with no double occupancy or holes. According to band theory, this would imply metallic behaviour. However, it turns out that the ground state of the Hubbard model is always insulating for finite values of U at half-filling [12, 29]. Thus, the model describes a Mott insulator that remains insulating for all U > 0, without undergoing a Mott transition.

Another important property is the separation of spin and charge degrees of freedom, which at halffilling occurs not only for low-energy states, but also extends to higher-energy excited states with any finite energy in the thermodynamic limit [12, 29]. The excitation spectrum consists of two types of elementary excitations: Charge excitations (holons and antiholons) carry charge but no spin, whereas spin excitations (spinons) carry spin but no charge. While the charge sector is gapped for any finite U, leading to the Mott insulating behaviour, the spin sector is massless [30], resulting in gapless modes [12]. Moreover, the spin correlations decay as power laws due to scale invariance [12, 30], indicating criticality. The model can indeed be described as a spin- $\frac{1}{2}$ Luttinger Liquid [29–31]. The dominant spin correlations exhibit quasi-long-range antiferromagnetic order at the wave vector $2k_F = \pi$, characteristic 2.2. Hubbard Model 7

of a spin density wave (SDW) [30, 32]. In the strong coupling limit $U \gg t_h$ the half-filled Hubbard chain maps onto the antiferromagnetic Heisenberg chain with exchange constant $J \sim 4t_h^2/U$ [30, 33]. For low-lying excitations it is therefore an effective spin system due to the finite charge gap. Notably, it has been shown that the critical behaviour of the half-filled Hubbard chain matches that of the antiferromagnetic Heisenberg chain for all U > 0, and not just in the strong coupling limit [34]. At U = 0, the Hubbard model corresponds to a spin-degenerate tight-binding band [33], which is metallic. In this work, the U = 0 case is only considered briefly.

2.2.2. η-Pairing and Off-Diagonal Long-Range Order

In addition to the particle-hole symmetry already mentioned, the Hamiltonian (2.18) also has two SU(2) symmetries [12]. Apart from rotational invariance in spin space, there is another hidden symmetry called η -pairing symmetry. This symmetry is especially interesting because it yields a potential mechanism of superconductivity [35, 36].

In order to reveal this symmetry, we must first introduce the η -operators

$$\hat{\eta}^{+} = \sum_{j} \underbrace{(-1)^{j} \hat{c}_{j,\downarrow}^{\dagger} c_{j,\uparrow}^{\dagger}}, \qquad \hat{\eta}^{-} = (\hat{\eta}^{+})^{\dagger} = \sum_{j} \underbrace{(-1)^{j} c_{j,\uparrow} c_{j,\downarrow}}_{\hat{\eta}_{j}^{-}}$$

$$(2.20)$$

$$\hat{\eta}^z = \sum_{j} \frac{1}{2} (\hat{n}_{j,\uparrow} + \hat{n}_{j,\downarrow} - 1), \qquad \hat{\eta}^2 = \frac{1}{2} (\hat{\eta}^+ \hat{\eta}^- + \hat{\eta}^- \hat{\eta}^+) + (\hat{\eta}^z)^2, \tag{2.21}$$

which satisfy the SU(2) commutation relations [12]

$$[\hat{\eta}^+, \hat{\eta}^-] = 2\hat{\eta}^z, \qquad [\hat{\eta}^z, \hat{\eta}^{\pm}] = \pm \hat{\eta}^{\pm}.$$
 (2.22)

Using these definitions and the fermion anticommutation relations (2.9) we can directly obtain the relations

$$[\hat{n}_{i,\sigma}, \hat{\eta}_i^+] = \delta_{ij}\eta_i^+, \qquad [\hat{n}_{i,\uparrow}\hat{n}_{i,\downarrow}, \hat{\eta}_i^+] = \delta_{ij}\eta_i^+. \tag{2.23}$$

This allows us to calculate

$$\left[-\mu \sum_{j} (\hat{n}_{j,\uparrow} + \hat{n}_{j,\downarrow}), \hat{\eta}^{+}\right] = -\mu \sum_{j} \left[(\hat{n}_{j,\uparrow} + \hat{n}_{j,\downarrow}), \hat{\eta}^{+}\right] = -\mu \sum_{j} \left[(\hat{n}_{j,\uparrow} + \hat{n}_{j,\downarrow}), \hat{\eta}_{j}^{+}\right] = -2\mu \,\hat{\eta}^{+}, \quad (2.24)$$

$$\left[U\sum_{j}\hat{n}_{j,\uparrow}\hat{n}_{j,\downarrow},\hat{\eta}^{+}\right] = U\sum_{j}\left[\hat{n}_{j,\uparrow}\hat{n}_{j,\downarrow},\hat{\eta}^{+}\right] = U\sum_{j}\left[\hat{n}_{j,\uparrow}\hat{n}_{j,\downarrow},\hat{\eta}_{j}^{+}\right] = U\hat{\eta}^{+}, \qquad (2.25)$$

$$\left[\frac{U}{4}L,\hat{\eta}^+\right] = 0. \tag{2.26}$$

Since we have set $\mu = U/2$ to achieve half-filling, the coulomb term \hat{H}_U of (2.18) commutes with $\hat{\eta}^+$. With the help of the fermion anticommutation relations (2.9), we also find:

where we assume L to be even.

This leads us to the essential property of the η -operators:

$$\left[\hat{H}, \hat{\eta}^{\pm}\right] = \left[\hat{H}, \hat{\eta}^{+} \hat{\eta}^{-}\right] = 0. \tag{2.28}$$

Since the number of spin up- and down electrons in \hat{H} is conserved, we also get

$$\left[\hat{H}, \hat{\eta}^z\right] = 0, \quad \left[\hat{H}, \hat{\eta}^2\right] = 0. \tag{2.29}$$

Consequently, any eigenstate of the Hubbard Hamiltonian \hat{H} is also an eigenstate $|\eta,\eta_z\rangle$ of both $\hat{\eta}^z$ and $\hat{\eta}^2$, with corresponding eigenvalues $\eta(\eta+1)$ and η^z . The $\hat{\eta}^+$ operator creates a so-called η -pair or doublon quasiparticle. $\hat{\eta}^-$ is the corresponding annihilation operator. From the momentum space representation $\hat{\eta}^+ = \sum_k \hat{c}^{\dagger}_{\pi-k,\downarrow} \hat{c}^{\dagger}_{k,\uparrow}$ it is easy to see that η -pairs carry a momentum of π .

This η -pairing mechanism in the Hubbard model was first proposed by Yang [13], who recognized that it can be used to construct exact eigenstates. Since the vacuum state $|0\rangle$ is a known eigenstate, many more can be generated by applying spin raising and lowering as well as η -pair creation and annihilation operators. Yang originally proposed the eigenstate $|\psi_N\rangle \propto (\hat{\eta}^+)^N |0\rangle$, containing 2N electrons and N η -pairs and showed that it has the exceptional property of possessing off-diagonal long-range order (ODLRO). The concept of ODLRO, also developed by Yang [17], is accepted as one possible definition of superconductivity since it implies the Meissner effect and flux quantization [17, 37, 38]. In contrast to conventional s-wave superconductivity, characterized by isotropic Cooper pairs with no phase difference, η -pairing features singlet pairs with a staggered phase of π .

For the Yang η -pairing states, ODLRO exists in the form of long-ranged pairing correlations [13]

$$\langle \hat{c}_{i,\uparrow} \hat{c}_{i,\downarrow} | \rho_2 | \hat{c}_{j,\uparrow} \hat{c}_{j,\downarrow} \rangle = \operatorname{Tr}(\hat{c}_{j,\uparrow} \hat{c}_{j,\downarrow} \rho \, \hat{c}_{i,\downarrow}^{\dagger} \hat{c}_{i,\uparrow}^{\dagger})$$

$$= \langle \psi_N | \hat{\eta}_i^+ \hat{\eta}_j^- | \psi_N \rangle (-1)^{i-j} = \frac{N(L-N)}{L(L-1)} (-1)^{i-j}$$
(2.30)

with $\rho = |\psi_N\rangle\langle\psi_N|$ and for $i \neq j$.

However, Yang also proved that such η -pairing states cannot be ground states but are excited states of the Hubbard model. The ground state therefore has $|\eta = 0, \eta_z = 0\rangle$.

Pair Correlation Function

For our numerical investigation, we use the real-space pair correlation function

$$P(r,t) = \frac{1}{L} \sum_{j} \langle \psi(t) | (\hat{\Delta}_{j+r}^{\dagger} \hat{\Delta}_{j} + \text{H. c.}) | \psi(t) \rangle, \qquad (2.31)$$

with the on-site singlet pair creation operator $\hat{\Delta}_{j}^{\dagger} = \hat{c}_{j,\downarrow}^{\dagger} \hat{c}_{j,\uparrow}^{\dagger}$, which is the same as the $\hat{\eta}_{j}^{+}$ operators except for the phase factor. A time dependency has been added here as this will be required later on. Note that at r = 0, the pair correlation corresponds to twice the double occupancy:

$$P(0,t) = 2n_d(t) = \frac{2}{L} \sum_{j} \langle \psi(t) | \hat{n}_{j,\uparrow} \hat{n}_{j,\downarrow} | \psi(t) \rangle.$$
 (2.32)

Most important in the context of η -pairing, however, is the Fourier transform $\widetilde{P}(q,t) = \sum_r e^{iqr} P(r,t)$ of the pair correlation function. Because η -pairs carry momentum $q=\pi$, the value $\widetilde{P}(\pi,t)$ serves as a key observable. For periodic boundary conditions or in the iMPS formalism, it satisfies the relation [14, 15]

$$\widetilde{P}(\pi,t) = \frac{2}{L} \langle \psi(t) | \hat{\eta}^{+} \hat{\eta}^{-} | \psi(t) \rangle. \tag{2.33}$$

For $|\eta, \eta_z\rangle$, $\widetilde{P}(\pi, t)$ is therefore $\frac{2}{L}[\eta(\eta + 1) - \eta_z(\eta_z - 1)]$, which makes the so-called pair structure factor ideal for detecting η -pairing in the system. Thus, $\widetilde{P}(\pi, t = 0) = 0$ for the ground state $|\eta = 0, \eta_z = 0\rangle$.

2.3. Entropy of Entanglement

Entanglement is one of the main distinctions between quantum and classical systems. Being able to measure the degree of entanglement in a system is therefore very useful, especially in strongly correlated systems. Von-Neumann entanglement entropy is one possible measure of the quantum entanglement between two subsystems of a pure bipartite quantum state [39, 40]. Given a system in a pure state $|\psi\rangle$, we divide it into two parts, A and B with Hilbert spaces \mathcal{H}_A and \mathcal{H}_B , so that $|\psi\rangle \in \mathcal{H}_A \otimes \mathcal{H}_B$. We then define the reduced density matrix for subsystem A as the partial trace of $\hat{\rho}_{AB} = |\psi\rangle\langle\psi|$ over B, given by

$$\hat{\rho}_A = \sum_{i}^{N_B} (\mathbb{1}_A \otimes \langle u_i |_B) (|\psi\rangle \langle \psi|) (\mathbb{1}_A \otimes |u_i\rangle_B) = \text{Tr}_B(\hat{\rho}_{AB})$$
(2.34)

with $N_B = \dim \mathcal{H}_B$. Now the entanglement entropy is just the von-Neumann entropy of $\hat{\rho}_A$:

$$S_A = S(\hat{\rho}_A) = -\operatorname{Tr}(\hat{\rho}_A \log \hat{\rho}_A) = -\operatorname{Tr}(\hat{\rho}_B \log \hat{\rho}_B) = S(\hat{\rho}_B) = S_B. \tag{2.35}$$

Although other measures of entanglement exist, the von-Neumann entanglement entropy is the most widely used measure in the context of iMPS. This is due to its direct link to the Schmidt decomposition and its applicability in finite-entanglement scaling. Many other measures also reduce to the von-Neumann entanglement entropy for pure states.

Schmidt Decomposition

Using the Schmidt decomposition, any pure state can be written as $|\psi\rangle = \sum_{i=1}^{m} \alpha_i |v_i\rangle_A \otimes |u_i\rangle_B$ where $m = \min\{N_A, N_B\}$ and $\{|v_1\rangle_A, \dots, |v_m\rangle_A\} \subset \mathcal{H}_A$, $\{|v_1\rangle_B, \dots, |v_m\rangle_B\} \subset \mathcal{H}_B$ orthonormal sets. In this representation, the reduced density matrices $\hat{\rho}_A$ and $\hat{\rho}_B$ are diagonal and the entanglement entropy is:

$$S_{A/B} = -\sum_{i=1}^{m} \alpha_i^2 \log \alpha_i^2.$$
 (2.36)

Written in this form, it is easy to see that $S_{A/B}$ becomes zero for a product state and is bounded by the maximum value $\log m$.

2.4. Dynamics and Non-Equilibrium

Due to the rapid progress of quantum simulators over the last two decades, the real-time dynamics of closed quantum many-body systems are now accessible experimentally $[1,\ 3-6]$. The active field of non-equilibrium dynamics promises to reveal new and interesting phenomena that do not exist within the constraints of equilibrium statistics.

Non-equilibrium dynamics is an expansive field, as there are many different ways to take a system out of equilibrium. In this work, we numerically investigate two possibilities within the context of the half-filled Hubbard model: a pump-probe approach, which we discuss in detail, and, more briefly, the dynamics following so-called quantum quenches.

2.4.1. Photoinduced Hubbard Model

Optical pumping is a technique that has been experimentally demonstrated to create new phases of quantum matter [41–45]. In particular, it was discovered that optical pulses can induce superconducting behaviour in high- T_c cuprates [46–49]. This led to a number of theoretical studies describing this phenomenon and showing that laser irradiation can give rise to nonequilibrium superconductivity in models of these materials [50–53]. One concept, frequently used for that description, is the η -pairing mechanism [14, 54–59].

Recent studies have specifically shown that pumping the Mott insulating phase of the half-filled Hubbard model can induce η -pairing-based superconductivity in the form of ODLRO [14, 15, 60]. This is possible because the pulse irradiation breaks the η -pairing symmetry, which allows the creation of η -pairs triggered by a nonlinear optical response. After the pulse, the symmetry is restored and the system contains a finite number of η -pairs. This non-equilibrium protocol will be the main focus of this thesis.

To model the laser pulse, the laser field must be added to the Hubbard Hamiltonian, making it time-dependent $\hat{H} \to \hat{H}(t)$.

Pump Pulse

To add a time-dependent external field, the kinetic part of the Hamiltonian (2.15) has to be modified, by adding the corresponding vector potential $\mathbf{A}(\hat{\mathbf{r}},t)$:

$$\left(\frac{\hat{\mathbf{p}}_i^2}{2m} + V_I(\hat{\mathbf{r}}_i)\right) \to \frac{1}{2m} \left(\hat{\mathbf{p}}_i + \frac{e\mathbf{A}(\hat{\mathbf{r}}_i, t)}{c}\right)^2 + V_I(\hat{\mathbf{r}}_i).$$
(2.37)

In second quantization, this leads to the Peierls substitution [12, 61] in the hopping term

$$t_h \hat{c}_{j,\sigma}^{\dagger} \hat{c}_{i,\sigma} \to t_h e^{ie\lambda_{i,j}/c} \hat{c}_{j,\sigma}^{\dagger} \hat{c}_{i,\sigma} \quad \text{with} \quad \lambda(\mathbf{r},t) = \int_{\mathbf{r}_j}^{\mathbf{r}_i} d\mathbf{r} \mathbf{A}(\mathbf{r},t).$$
 (2.38)

We set the lattice spacing $|\mathbf{r}_i - \mathbf{r}_j|$, Plank constant \hbar , elementary charge e and speed of light c to 1. Additionally, since the wavelength is much larger than the lattice spacing, the vector potential is approximated to be independent of \mathbf{r} . Using $\mathbf{A}(t) = A(t)\mathbf{e}_x$ parallel to the one-dimensional chain direction, this gives us the substitutions for (2.18):

$$t_h \hat{c}_{j,\sigma}^{\dagger} \hat{c}_{j+1,\sigma} \to t_h e^{iA(t)} \hat{c}_{j,\sigma}^{\dagger} \hat{c}_{j+1,\sigma} \tag{2.39a}$$

$$t_h \hat{c}_{j+1,\sigma}^{\dagger} \hat{c}_{j,\sigma} \to t_h e^{-iA(t)} \hat{c}_{j+1,\sigma}^{\dagger} \hat{c}_{j,\sigma},$$
 (2.39b)

making the Hamiltonian time-dependent.

We use the vector potential

$$A(t) = A_0 e^{-(t-t_0)^2/(2\sigma_p^2)} \cos\left[\omega_p(t-t_0)\right], \tag{2.40}$$

to model a pump pulse with amplitude A_0 and frequency ω_p . It is centered at time t_0 (> 0) and has a width σ_p . An example of the pump pulse described above is illustrated in Fig. 2.1.

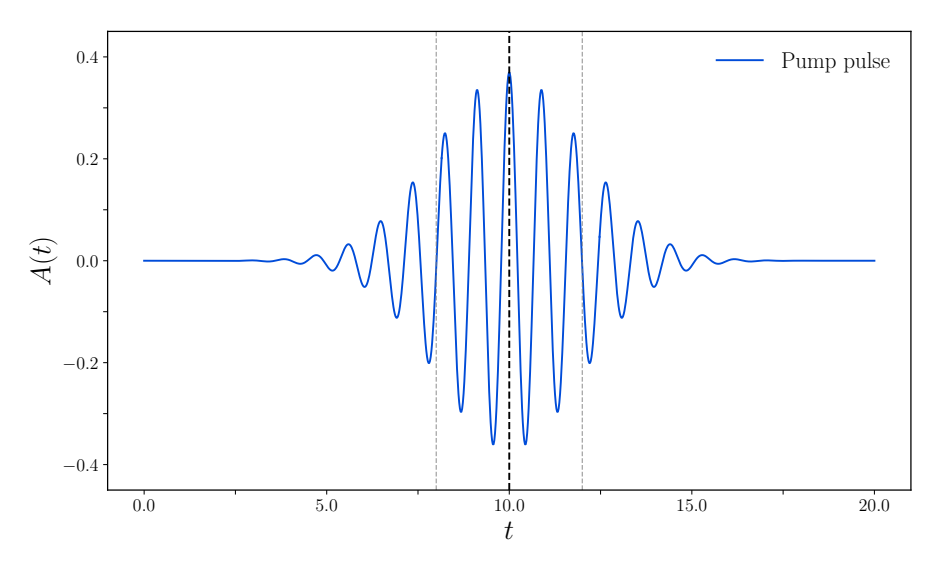


Figure 2.1.: Illustration of the pump pulse as modeled by (2.40). The pulse is centered at $t_0 = 10$, has a width of $\sigma_p = 2$, an amplitude of $A_0 = 0.37$, and a frequency of $\omega_p/t_h = 7.1$. The black dashed line represents the center of the pulse, while the grey dashed lines denote the width.

2.4.2. Quantum Quenches

Quantum quenches are the simplest way to take a system out of equilibrium and refer to a change of the system parameters. Although there are slow quenches, the term usually refers to a sudden change in one of the system parameters. Starting from the ground state of a Hamiltonian \hat{H}_0 the system dynamically evolves under a changed Hamiltonian \hat{H} :

$$\hat{H}_{\text{quench}} = \begin{cases} \hat{H}_0 & t < 0, \\ \hat{H} & t \ge 0. \end{cases}$$
 (2.41)

Such a quench is a relatively generic concept, but there is currently particular interest in studying quenches near or across an equilibrium quantum phase transition. This is because these quenches can lead to what are known as dynamical quantum phase transitions (DQPTs).

2.4.3. Dynamical Quantum Phase Transitions

DQPTs are a relatively new concept that was first introduced in Ref. [19]. The term describes a non-equilibrium phenomenon that generalizes equilibrium quantum phase transitions to real-time dynamics. DQPTs typically arise in systems undergoing a (sudden) quantum quench, but have since been extended to other non-equilibrium protocols [62–69]. The signature of a DQPT (although not yet under this name) was actually first discovered during a slow quench in Ref. [70]. In this thesis, we will look for DQPTs in the photoinduced Hubbard model. While the photo-pulse protocol is our focus, we begin by introducing the concept of DQPTs through the simpler and well-studied quench protocol. This also gives us a benchmark comparison for the more complex photo excitation protocol.

The key quantity of study is the Loschmidt (or return) amplitude defined as

$$\mathcal{G}(t) = \langle \psi_0 | \psi_0(t) \rangle = \langle \psi_0 | e^{-i\hat{H}t} | \psi_0 \rangle. \tag{2.42}$$

where $|\psi_0\rangle$ is the ground state of the initial Hamiltonian \hat{H}_0 and $|\psi_0(t)\rangle = e^{-i\hat{H}t}|\psi_0\rangle$ is the time evolved non-equilibrium state according to the quench protocol (2.41).

The corresponding (return-)probability

$$\mathcal{L}(t) = |\mathcal{G}(t)|^2 \tag{2.43}$$

is called Loschmidt echo and quantifies the probability of the system returning to its initial state. The Loschmidt amplitude $\mathcal{G}(t)$ can formally be interpreted as a boundary partition function $Z(z) = \langle \psi_A | e^{-z\hat{H}} | \psi_B \rangle$ with a complex parameter z = it. For $z \in \mathbb{R}$, Z(z) is the partition function of the field theory described by \hat{H} with boundary conditions encoded in the boundary states $|\psi_A\rangle$ and $|\psi_B\rangle$ [71]. The initial state $|\psi_0\rangle$ can therefore be interpreted as a boundary condition in time. While a boundary partition function with a complex parameter doesn't describe a physical system, this interpretation has been used to apply concepts from equilibrium statistical mechanics to the Loschmidt amplitude. In particular, the analysis of partition function zeros in the complex temperature plane, originally introduced by Fisher [72], has played an important role. It also motivates the definition of a rate function of the return amplitude g(t),

$$\mathcal{G}(t) = e^{-Lg(t)} \tag{2.44}$$

with $L \gg 1$ the number of sites. Consequently, the return probability can be expressed as

$$\mathcal{L}(t) = e^{-L\lambda(t)},\tag{2.45}$$

with the return probability rate function per site in the thermodynamic limit:

$$\lambda(t) = -\lim_{L \to \infty} \frac{1}{L} \log \mathcal{L}(t) = 2 \Re(g(t)). \tag{2.46}$$

Due to the connection to partition functions, $\lambda(t)$ can also be viewed as the dynamical analog to a free energy density. This is however only a formal similarity. It is not a thermodynamic property from which physical observables can be derived.

Nevertheless, by analogy with the theory of equilibrium (quantum) phase transitions, where non-analyticities in the free energy signal phase transitions, a DQPT is defined as a non-analytic point of the Loschmidt amplitude as a function of time [18]. In the context of Fisher zeros, this occurs when a region of such zeros crosses the real-time axis in the thermodynamic limit. DQPTs are therefore phase transitions in time instead of as a function of a control parameter. Most of the time, DQPTs occur when quenching across an underlying equilibrium phase transition. In one-dimensional systems this mostly leads to a rate function of the form

$$\lambda(t) \sim \left| \frac{t - t_c}{t_c} \right| \tag{2.47}$$

around a critical time t_c .

Example: DQPT in the Transverse Field Ising Model

To illustrate this behaviour, we consider the simplest example in the form of the one-dimensional transverse field Ising model [73]. This model describes a quantum-mechanical spin chain with nearest-neighbour interactions in a magnetic field that is perpendicular to the axis of the spin-spin coupling. The Hamiltonian is given by

$$\hat{H}_{\text{TI}} = -J \sum_{\langle i,j \rangle} \hat{\sigma}_i^z \hat{\sigma}_j^z + g \sum_j \hat{\sigma}_j^x, \tag{2.48}$$

where J is the interaction strength and g is the strength of the transverse magnetic field.

For |J/g| > 1, the spin-spin interactions dominate and the system is in an ordered phase (ferromagnetic for J > 0, antiferromagnetic for J < 0). For |J/g| < 1, the transverse field dominates and the system is in a paramagnetic disordered phase. The system therefore undergoes a quantum phase transition at |J/g| = 1. If the system is quenched across this equilibrium phase transition, the rate function (2.46) for the Loschmidt echo exhibits a clear non-analytic cusp, signaling the occurrence of a DQPT, as shown in Fig. 2.2.

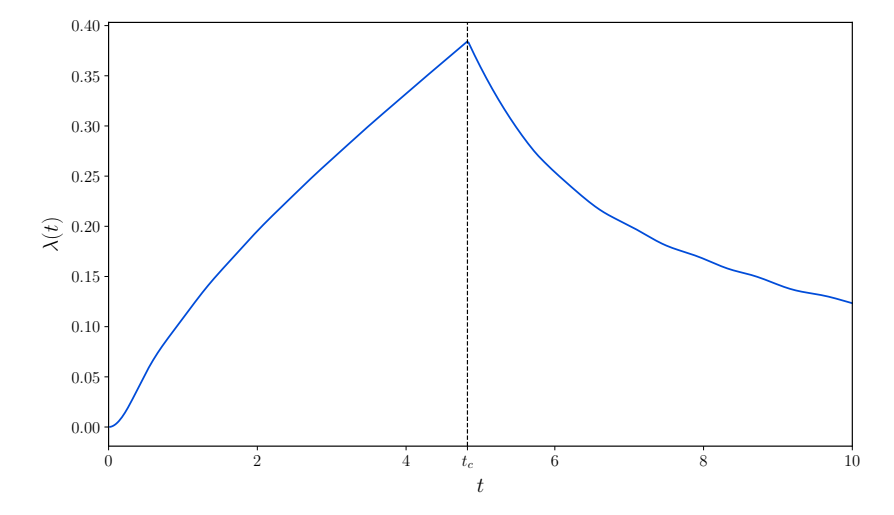


Figure 2.2.: Time evolution of the rate function $\lambda(t)$ following a quantum quench across the equilibrium phase transition in the transverse field Ising model. The system was quenched from $g_0 = 0.8$ to g = 1.2 with $J_0 = J = 1$. The ground state and subsequent time evolution were computed using the iTEBD algorithm, which will be discussed in the next chapter. The cusp is the signature of a DQPT.

For specific quenches, it is even possible to demonstrate analytically, by employing renormalization group (RG) techniques, that DQPTs in the one- and two-dimensional Ising model exhibit the same scaling behaviour and universality class as their equilibrium counterparts [74]. In one dimension, this correspondence arises because, in these cases, the Loschmidt amplitude is equivalent to the classical equilibrium partition function but with a complex effective coupling. As a result, the DQPTs map to the unstable fixed point of the equilibrium Ising model. While in the two-dimensional case there is no exact RG transformation, the exact solution of the model can nevertheless be extended to complex couplings.

Exceptions, Special Cases, and Generalizations

DQPTs can also occur without quenching across an equilibrium phase transition and not occur despite quenching across an equilibrium phase transition [18]. A notable exception are noninteracting topological systems: here, a DQPT always appears whenever a topological phase transition is crossed, specifically in one dimension or in two dimensions if the Chern number changes [18]. In these cases, one can even define dynamical order parameters, such that the DQPT separates distinct "dynamical phases" [75]. Nonetheless, while there is a profound connection between equilibrium phase transitions and non-equilibrium quantum phase transitions, DQPTs are, in general, an independent non-equilibrium phenomenon. Notably, DQPTs have also been observed experimentally in several quantum simulators [76–81].

For more general non-equilibrium protocols beyond quenches, the Loschmidt amplitude can be generalized as

$$\mathcal{G}(t) = \langle \psi_0 | \hat{U}(t) | \psi_0 \rangle \tag{2.49}$$

with the unitary time evolution operator $\hat{U}(t)$ generated by the time-depended Hamiltonian.

3. Numerical Methods

3.1. Tensor Networks

Tensor networks have proven to be powerful and versatile tools for simulating quantum many body systems and especially strongly correlated systems. In this section, we provide a brief introduction to the concept of tensor networks and matrix product states (MPS) and then discuss infinite matrix product states (iMPS) in greater detail. For a detailed overview of tensor operations such as contraction, tracing, and singular value decomposition (SVD), please refer to Ref. [82, Chapter 1]. Other useful introductions to this topic include the reviews and lecture notes in Refs. [7, 8, 83–86].

Let's consider an N-particle quantum many-body system, where each particle has $d = \dim \mathcal{H}_1$ basis states. In section 2.1 we have seen that any pure state of such a system can be written as

$$|\psi\rangle = \sum_{i_1,\dots,i_N=1}^d C^{i_1,\dots,i_N} |u_{i_1}^{(1)}\rangle \otimes |u_{i_2}^{(2)}\rangle \otimes \dots \otimes |u_{i_N}^{(N)}\rangle$$
(3.1)

with a single-particle basis $\{|u_{i_j}^{(j)}\rangle\}$ for each one-particle Hilbert space $\mathcal{H}_1^{(j)}$ and $i_j=1,\ldots,d$. The complex coefficients C^{i_1,\ldots,i_N} can be interpreted as a rank-N tensor C with N indices where each index can take up to d different values. For our needs, a tensor is therefore simply a multidimensional array. This tensor can be represented diagrammatically as in Fig. 3.1, where each leg corresponds to an (open) index.

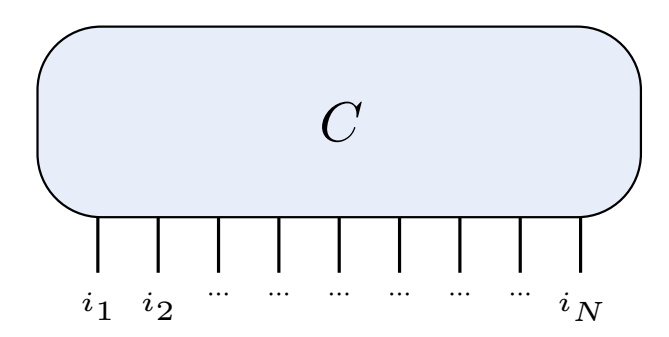


Figure 3.1.: Graphical representation of an rank-N tensor C.

In this diagrammatic language, tensors are represented by geometric shapes with lines or *legs* representing their indices. When two tensors are combined by summing over one or more of their indices, the corresponding legs in the diagram are connected. This operation is referred to as a contraction.

3.1.1. Matrix Product States

In case of the one-band Hubbard model, each index corresponds not to one particle, but to one lattice site. The basis states for each site are given by $\{|0\rangle, |\uparrow\rangle, |\downarrow\rangle, |\uparrow\downarrow\rangle\}$, and thus the local Hilbert space has dimension d=4. This implies that we would need $\mathcal{O}(4^L)$ coefficients to represent the quantum state of a system with L lattice sites. This exponential growth of the Hilbert space in system size quickly becomes computationally infeasible, making it necessary to find a more efficient way to represent $|\psi\rangle$.

This is where tensor networks, and in particular MPS for one-dimensional systems, come in. The key idea, as illustrated in Fig. 3.2, is to use a network of smaller tensors rather than a single large tensor. In our example, the network consists of five tensors, which are interconnected via *contracted* indices. Each unmatched leg still corresponds to an index, associated with the physical degrees of freedom of that site. Starting from a general rank-N tensor, the MPS representation can be constructed using successive SVDs.

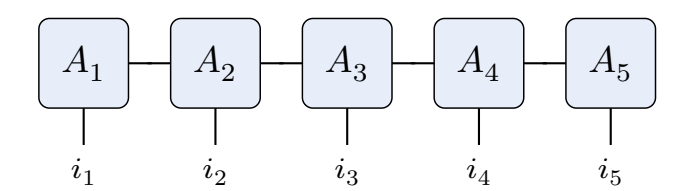


Figure 3.2.: Graphical depiction of a tensor network in the form of a MPS for five sites.

Using this MPS representation, we now have a handle to limit the number of parameters by bounding the so-called bond dimension χ of the contracted indices. For a chain with of L sites, the MPS parameterizes the system with only $\mathcal{O}(L\chi^2d)$ parameters, which is exponentially fewer than the $\mathcal{O}(4^L)$ parameters for the exact representation. By restricting χ , we effectively truncate the smallest singular values (Schmidt coefficients) in the SVD of the state at each bipartition [82]. The maximum entanglement entropy that can be represented is therefore bounded by $\log \chi$, making the MPS framework particularly efficient for states with limited entanglement.

Area Law

The area law is a fundamental property of the entanglement entropy that is essential for the relevance of MPS. It states that for a low energy eigenstate of a gapped Hamiltonian with only local interactions, the entanglement entropy $S(\hat{\rho}_A)$ of a connected region A scales as the size of its boundary [87]. For a bipartition of a one-dimensional chain, the area law therefore predicts that the entanglement entropy is independent of system size:

$$S_A \sim \mathcal{O}(1).$$
 (3.2)

For a gapless or critical one-dimensional system, however, the entanglement entropy scales as [88, 89]

$$S_A \sim \text{const.} \cdot \log l + \mathcal{O}(1)$$
 (3.3)

with l the size of the subsystem A. The entanglement entropy of excited states can even scale with the volume of the subsystem [90–92].

Any MPS with finite bond dimension χ can therefore efficiently represent ground states of gapped systems, because the maximal entanglement entropy across any cut is upper bounded. This makes MPS a natural and efficient ansatz for such states. In contrast, highly entangled states, such as those found in critical one-dimensional systems like the repulsive Hubbard model, require an MPS with a bond dimension that grows polynomially with system size to accurately capture the logarithmic scaling of entanglement entropy.

3.1. Tensor Networks 17

3.1.2. Infinite Matrix Product States

To work directly in the thermodynamic limit $L \to \infty$, the conventional MPS ansatz must be extended to the iMPS representation, as introduced in Refs. [8, 10, 85]. By exploiting translational invariance, the state of an infinite chain can be efficiently represented by repeating a finite unit cell of tensors. In this section, we introduce the basics of the iMPS representation for the simplest case of a single-site unit cell, consisting of a tensor $A^i \in \mathbb{C}^{\chi \times \chi}$ for each physical index $i_j = 1, \ldots, d$. The state can be written as

$$|\psi(A)\rangle = \sum_{\{i_n\}} \cdots A^{i_{-1}} A^{i_0} A^{i_1} \cdots | \cdots u_{i-1} u_{i_0} u_{i+1} \cdots \rangle.$$
 (3.4)

The diagrammatic representation of such a state is

$$|\psi(A)\rangle = \dots - A \qquad A \qquad A \qquad A \qquad A \qquad \dots$$
 (3.5)

This concept can be generalized to unit cells containing multiple sites, which we will do in the next section on algorithms.

One central object in many calculations is the transfer matrix or transfer operator defined as

$$E(X) = \sum_{i=1}^{d} A^{i} X(A^{i})^{\dagger}.$$
 (3.6)

For a properly normalized iMPS, the transfer matrix has a leading eigenvalue $\lambda_1 = 1$ with left and right fixed points l, r fulfilling Tr(lr) = 1:

$$E(r) = \sum_{i} A^{i} r (A^{i})^{\dagger} = r$$
 $E^{\dagger}(l) = \sum_{i} (A^{i})^{\dagger} l A^{i} = l$. (3.7)

From now on, we will switch to the diagrammatic language for its simplicity. Here, the eigenvalue equations are

Canonical Forms

Notice that the state $|\psi(A)\rangle$ is invariant under the gauge transform $A^{ij} \to X^{-1}A^{ij}X$. Consequently, the tensor A is not uniquely defined by the state. To address this, we make use of this gauge freedom, together with the fixed points of the transfer matrix, to define canonical forms. These are very useful both conceptually and computationally.

First we decompose the fixed points as $l = L^{\dagger}L$ and $r = RR^{\dagger}$. This allows us to express the state in left-canonical form using the tensor $A_L = LAL^{-1}$, or in right-canonical form using the tensor $A_R = R^{-1}AR$. In left- or right-canonical form, the corresponding transfer matrices of A_L and A_R have the identity matrix 1 as their left or right fixed point, respectively. A_L is thus a left-normalized tensor,

while A_R is right-normalized. With the help of a new tensor C = LR we arrive at the mixed-canonical form

$$|\psi(A)\rangle = \dots - A_L - A_L - C - A_R - A_R - \dots$$
 (3.9)

The matrix C can additionally be diagonalized using an SVD, $C = USV^{\dagger}$, where the unitary matrices U and V^{\dagger} can be absorbed into new definitions of A_L and A_R . With this, we see a major advantage of the canonical form for the first time: the diagonal elements $C_{i,i}$ are the Schmidt coefficients, and the entropy of entanglement can be directly read off as

$$S_{L/R} = -\sum_{i=1}^{\chi} C_{i,i}^{2} \log C_{i,i}^{2}.$$
 (3.10)

Since the chain is translation invariant, the entanglement entropy is the same at every cut. However, it does depend on the bond dimension χ , and we therefore write $S_{\chi} = S_{L/R}$. In particular, as in the finite case, the entanglement entropy is bounded from above by $\log \chi$.

Expectation Values and Overlaps

To calculate the expectation value (per site) of an operator \hat{H} , the approach of the finite-size case can be transferred, and the calculation becomes

$$\langle \psi(A)|\hat{H}|\psi(A)\rangle = \begin{pmatrix} C & A_R & A_R \\ & \hat{H} & & \\ & C^\dagger & A_R^\dagger & A_R^\dagger & & \\ & & & & \\ & & & & \\ & & & & \\ & & & & \\ & & & & \\ & & & & \\ & & & & \\$$

All the infinitely many sites on which the operator does not act are contracted away using the corresponding left and right fixed points.

The norm of a state is then accordingly computed as

$$\langle \psi(A)|\psi(A)\rangle = \begin{array}{c} A & A \\ \hline A^{\dagger} & A^{\dagger} \end{array} = \begin{array}{c} A \\ \hline A^{\dagger} & A^{\dagger} \end{array} = \begin{array}{c} A \\ \hline A^{\dagger} & A^{\dagger} \end{array} = \begin{array}{c} A \\ \hline A^{\dagger} & A^{\dagger} \end{array} = \begin{array}{c} A \\ \hline A^{\dagger} & A^{\dagger} \end{array} = \begin{array}{c} A \\ \hline A^{\dagger} & A^{\dagger} \end{array} = \begin{array}{c} A \\ \hline A^{\dagger} & A^{\dagger} \end{array} = \begin{array}{c} A \\ \hline A^{\dagger} & A^{\dagger} \end{array} = \begin{array}{c} A \\ \hline A^{\dagger} & A^{\dagger} \end{array} = \begin{array}{c} A \\ \hline A^{\dagger} & A^{\dagger} \end{array} = \begin{array}{c} A \\ \hline A^{\dagger} & A^{\dagger} \end{array} = \begin{array}{c} A \\ \hline A^{\dagger} & A^{\dagger} \end{array} = \begin{array}{c} A \\ \hline A^{\dagger} & A^{\dagger} \end{array} = \begin{array}{c} A \\ \hline A^{\dagger} & A^{\dagger} \end{array} = \begin{array}{c} A \\ \hline A^{\dagger} & A^{\dagger} \end{array} = \begin{array}{c} A \\ \hline A^{\dagger} & A^{\dagger} \end{array} = \begin{array}{c} A \\ \hline A^{\dagger} & A^{\dagger} \end{array} = \begin{array}{c} A \\ \hline A^{\dagger} & A^{\dagger} \end{array} = \begin{array}{c} A \\ \hline A^{\dagger} & A^{\dagger} \end{array} = \begin{array}{c} A \\ \hline A^{\dagger} & A^{\dagger} \end{array} = \begin{array}{c} A \\ \hline A^{\dagger} & A^{\dagger} \end{array} = \begin{array}{c} A \\ \hline A^{\dagger} & A^{\dagger} \end{array} = \begin{array}{c} A \\ \hline A^{\dagger} & A^{\dagger} \end{array} = \begin{array}{c} A \\ \hline A^{\dagger} & A^{\dagger} \end{array} = \begin{array}{c} A \\ \hline A^{\dagger} & A^{\dagger} \end{array} = \begin{array}{c} A \\ \hline A^{\dagger} & A^{\dagger} \end{array} = \begin{array}{c} A \\ \hline A^{\dagger} & A^{\dagger} \end{array} = \begin{array}{c} A \\ \hline A^{\dagger} & A^{\dagger} \end{array} = \begin{array}{c} A \\ \hline A^{\dagger} & A^{\dagger} \end{array} = \begin{array}{c} A \\ \hline A^{\dagger} & A^{\dagger} \end{array} = \begin{array}{c} A \\ \hline A^{\dagger} & A^{\dagger} \end{array} = \begin{array}{c} A \\ \hline A^{\dagger} & A^{\dagger} \end{array} = \begin{array}{c} A \\ \hline A^{\dagger} & A^{\dagger} \end{array} = \begin{array}{c} A \\ \hline A^{\dagger} & A^{\dagger} \end{array} = \begin{array}{c} A \\ \hline A^{\dagger} & A^{\dagger} \end{array} = \begin{array}{c} A \\ \hline A^{\dagger} & A^{\dagger} \end{array} = \begin{array}{c} A \\ \hline A^{\dagger} & A^{\dagger} \end{array} = \begin{array}{c} A \\ \hline A^{\dagger} & A^{\dagger} \end{array} = \begin{array}{c} A \\ \hline A^{\dagger} & A^{\dagger} \end{array} = \begin{array}{c} A \\ \hline A^{\dagger} & A^{\dagger} \end{array} = \begin{array}{c} A \\ \hline A^{\dagger} & A^{\dagger} \end{array} = \begin{array}{c} A \\ \hline A^{\dagger} & A^{\dagger} \end{array} = \begin{array}{c} A \\ \hline A^{\dagger} & A^{\dagger} \end{array} = \begin{array}{c} A \\ \hline A^{\dagger} & A^{\dagger} \end{array} = \begin{array}{c} A \\ \hline A^{\dagger} & A^{\dagger} \end{array} = \begin{array}{c} A \\ \hline A^{\dagger} & A^{\dagger} \end{array} = \begin{array}{c} A \\ \hline A^{\dagger} & A^{\dagger} \end{array} = \begin{array}{c} A \\ \hline A^{\dagger} & A^{\dagger} \end{array} = \begin{array}{c} A \\ \hline A^{\dagger} & A^{\dagger} \end{array} = \begin{array}{c} A \\ \hline A^{\dagger} & A^{\dagger} \end{array} = \begin{array}{c} A \\ \hline A^{\dagger} & A^{\dagger} \end{array} = \begin{array}{c} A \\ \hline A^{\dagger} & A^{\dagger} \end{array} = \begin{array}{c} A \\ \hline A^{\dagger} & A^{\dagger} \end{array} = \begin{array}{c} A \\ \hline A^{\dagger} & A^{\dagger} \end{array} = \begin{array}{c} A \\ \hline A^{\dagger} & A^{\dagger} \end{array} = \begin{array}{c} A \\ \hline A^{\dagger} & A^{\dagger} \end{array} = \begin{array}{c} A \\ \hline A^{\dagger} & A^{\dagger} \end{array} = \begin{array}{c} A \\ \hline A^{\dagger} & A^{\dagger} \end{array} = \begin{array}{c} A \\ \hline A^{\dagger} & A^{\dagger} \end{array} = \begin{array}{c} A \\ \hline A^{\dagger} & A^{\dagger} \end{array} = \begin{array}{c} A \\ \hline A^{\dagger} & A^{\dagger} \end{array} = \begin{array}{c} A \\ \hline A^{\dagger} & A^{\dagger} \end{array} = \begin{array}{c} A \\ \hline A^{\dagger} & A^{\dagger} \end{array} = \begin{array}{c} A \\ \hline A^{\dagger} & A^{\dagger} \end{array} = \begin{array}{c} A \\ \hline A^{\dagger} & A^{\dagger} \end{array} = \begin{array}{c} A \\ \hline A^{\dagger} & A^{\dagger} \end{array} = \begin{array}{c} A \\ \hline A^{\dagger} & A^{\dagger} \end{array} = \begin{array}{c} A \\ \hline A^{\dagger} & A^{\dagger} \end{array} = \begin{array}{c} A \\ \hline A^{\dagger} & A^{\dagger} \end{array} = \begin{array}{c} A \\ \hline A^{\dagger} & A^{\dagger}$$

Now it is also clear why the iMPS is normalized the way it is.

However, if we want to calculate the overlap between two different states $|\psi(A)\rangle$ and $|\psi(B)\rangle$, it vanishes exponentially with system size in the thermodynamic limit. This is because the largest eigenvalue ϵ_1 of the mixed transfer matrix $E(X) = \sum_i A^i X(B^i)^{\dagger}$ is strictly less than one, provided the two states are not related by a gauge transformation. This phenomenon is known as the orthogonality catastrophe, according to which different states in the thermodynamic limit become orthogonal.

To compute the Loschmidt amplitude (2.42) in this context, we interpret the leading eigenvalue $\epsilon_1(t)$ as the overlap per site [8, 93, 94]. The rate function (2.46) is then computed as

$$\lambda(t) = -2\log|\epsilon_1(t)|. \tag{3.13}$$

3.1. Tensor Networks 19

Correlation Functions

With this knowledge we can now also compute two point correlation functions $\langle \psi(A)|\hat{O}_{\alpha}^{(i)}\hat{O}_{\beta}^{(j)}|\psi(A)\rangle$ as

which only depends on the distance |i-j| because of translation invariance. We can now add the identity $\mathbb{1} = \sum_i |\lambda_i\rangle\langle\lambda_i\rangle$ into the correlation function, where $|\lambda_i\rangle$ and $|\lambda_i|$ are the biorthogonal right and left eigenvectors of the transfer matrix for eigenvalues $|\lambda_i|$ [8]. As we have already seen, $|\lambda_1| = 1$, $|\lambda_1| = r$ and $|\lambda_1| = l$. This reduces the transfer matrices to a product of the corresponding eigenvalue in every summand and the correlation function can be written as [8, 10]

$$C_{\alpha,\beta}(|i-j|) = \underbrace{l}_{A^{\dagger}} \underbrace{\hat{O}_{\alpha}}_{A^{\dagger}} r \times \underbrace{l}_{i\geq 2} (\lambda_{i})^{m-n-1} \underbrace{l}_{0} \underbrace{\hat{O}_{\alpha}}_{A^{\dagger}} \times \lambda_{i} \underbrace{\hat{O}_{\beta}}_{A^{\dagger}} r. \quad (3.15)$$

Any correlation function of an iMPS therefore consists of a long-range disconnected part and a connected part that is a sum of exponentials. Power-law correlations cannot be captured natively, and long-range correlations only exist if $\langle \hat{O}_{\alpha}^{(i)} \rangle$ and $\langle \hat{O}_{\beta}^{(j)} \rangle$ are non vanishing. In case of the pair correlation function (2.31), the disconnected part is zero because the half-filled

In case of the pair correlation function (2.31), the disconnected part is zero because the half-filled Hubbard model is particle-number-conserving. Thus, the ODLRO of η -pairing states can only be approximated by the exponentially decaying connected part of the correlation function.

To characterize the decay of the connected part, we define the correlation length in terms of the second-largest eigenvalue of the transfer matrix as

$$\xi = -\frac{1}{\log|\lambda_2|}.\tag{3.16}$$

Since the value of the correlation length generally depends on the bond dimension χ , we write ξ_{χ} .

3.2. Algorithms

All tensor network calculations were performed using the Julia language with the work-in-progress ITensorInfiniteMPS.jl package [95], based on the ITensors.jl library [96–98].

3.2.1. iTEBD

The infinite time-evolving block decimation algorithm (iTEBD), first proposed in 2006 by Vidal [9], allows the simulation of an infinite one-dimensional quantum lattice systems. The algorithm is based on the TEBD algorithm [99, 100] and makes use of translational invariance and parallelizability of local updates in TEBD to work directly in the thermodynamic limit. In this way, extrapolations using finite-size scaling can be omitted.

Starting with an initial state $|\psi_0\rangle$, iTEBD can be used for a real-time evolution

$$|\psi(t)\rangle = \exp(-i\hat{H}t)|\psi_0\rangle,$$
 (3.17)

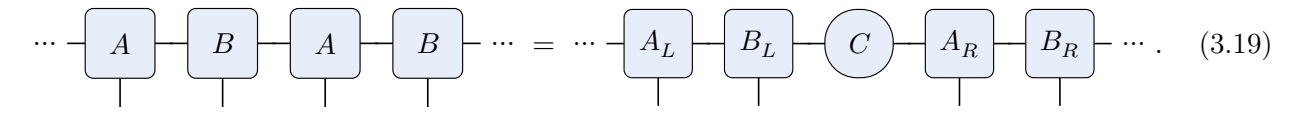
as well as for an imaginary time evolution to find the ground state $|\psi_{GS}\rangle$ of the Hamiltionian \hat{H} :

$$|\psi_{GS}\rangle = \lim_{t \to \infty} \frac{\exp(-\hat{H}t)|\psi_0\rangle}{\|\exp(-\hat{H}t)|\psi_0\rangle\|}.$$
 (3.18)

We use iTEBD for all our real-time evolutions and some ground-state computations.

Gamma-Lambda Notation

Before presenting the algorithm, we first extend the unit cell to include two sites in order to maintain translational invariance when applying a two-site operator that represents nearest-neighbour interactions:



It is also useful to introduce the $\Gamma\Lambda$ notation for iMPS, which can easily be obtained using SVDs [86]. In this form, the state is described by tensors Γ and diagonal matrices Λ containing the Schmidt coefficients. The relationship between the mixed-canonical form and the $\Gamma\Lambda$ notation for a two-site unit cell, which we will use as the definition of the $\Gamma\Lambda$ notation, is

The Algorithm

To perform the imaginary time evolution of an iMPS, the operator $\hat{U}(t) = e^{-t\hat{H}}$ has to be applied to the state. For a real-time evolution, the following algorithm remains identical except that the operator becomes $\hat{U}(t) = e^{-it\hat{H}}$. To apply the time evolution operator, we start by splitting the Hamiltonian \hat{H} with nearest-neighbour interactions into two parts, containing the odd and even bonds respectively:

$$\hat{H} = \sum_{j} \hat{h}^{[j,j+1]} = \sum_{j} \hat{h}^{[2j,2j+1]} + \sum_{j} \hat{h}^{[2j-1,2j]} = \hat{H}_{\text{even}} + \hat{H}_{\text{odd}}.$$
 (3.21)

3.2. Algorithms 21

The on-site Coulomb interaction of the Hubbard model can be arbitrarily divided between the two parts. Using a second-order Suzuki-Trotter decomposition [101], $\hat{U}(t)$ can then be written as

$$\hat{U}(t) = e^{-t\hat{H}} = e^{-\tau N\hat{H}} = \left[e^{-\tau(\hat{H}_e + \hat{H}_o)} \right]^N = \left[e^{-(\tau/2)\hat{H}_o} e^{-\tau\hat{H}_e} e^{-(\tau/2)\hat{H}_o} + \mathcal{O}(\tau^3) \right]^N.$$
(3.22)

Since the individual terms in both the even and the odd sum commute with each other, the exponentials can easily be computed as products of two-site gates corresponding to the local exponentiated Hamiltonian terms. Time evolution is then achieved by repeatedly applying the three operators and due to translation invariance, only two sites need to be updated in each application. The error grows with the time-step size and accumulates over the course of the simulation. A fourth-order Suzuki-Trotter decomposition would reduce the error per step to $\mathcal{O}(\tau^5)$ but also requires the application of seven operators per step instead of three [101].

After applying a gate, the $\Gamma\Lambda$ iMPS structure is destroyed and needs to be restored. The original version [9, 102] of the iTBED algorithm requires the inversion of singular value matrices, potentially leading to numerical instabilities, to achieve this. Therefore, we use a modified algorithm following Hastings [103]. The procedure for updating an odd bond after applying $\hat{U}_{\rm o} = e^{-(\tau/2)\hat{H}_{\rm o}}$ is illustrated in Fig. 3.3.

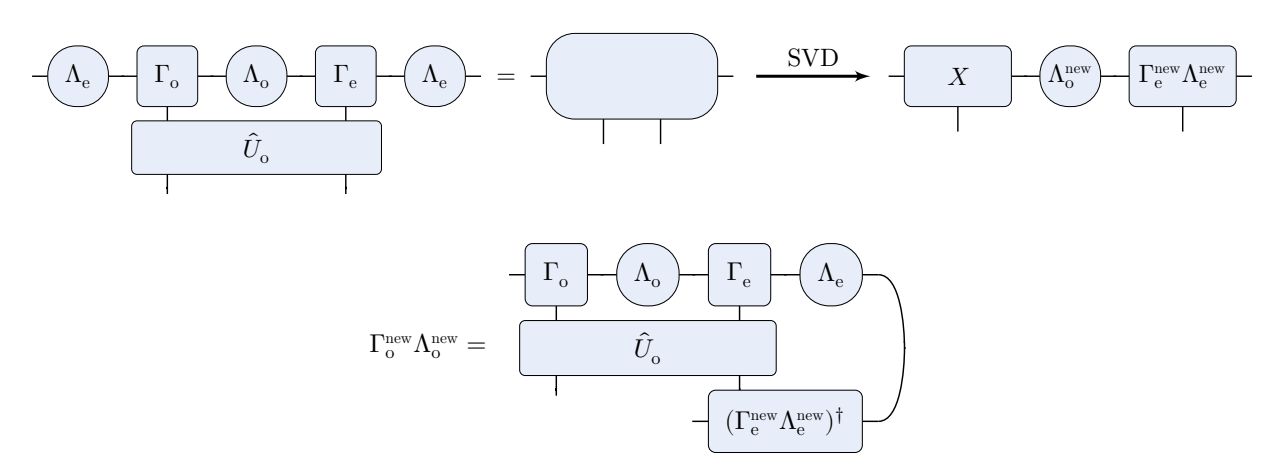


Figure 3.3.: Updating steps of the iMPS after applying U_o . Notice that after this update procedure, we do not know the individual tensors Γ_e and Γ_o but only $\Gamma_e\Lambda_e$ and $\Gamma_o\Lambda_o$. This is, however, not a problem because Λ_e and Λ_o are updated individually, which is sufficient to compute the entanglement entropy, expectation values, and the eigenvalues of the transfer matrix.

To control the size of the iMPS, only the largest χ singular values are kept after the SVD. A major advantage of this algorithm is that both storage and computational costs are independent of system size. However, for ground-state computations, there are more efficient algorithms.

3.2.2. VUMPS

For the computation of ground states, we also use the VUMPS (variational uniform matrix product states) algorithm [10, 11], which efficiently computes ground states of one-dimensional systems in the thermodynamic limit. VUMPS is used because it typically converges significantly faster and is more accurate than iTEBD, especially for critical systems. It variationally updates the iMPS through eigenvalue problems to minimize the energy until convergence is reached. We use the existing implementation in the ITensorInfiniteMPS.jl package [95] and will not discuss the internal workings of the algorithm in this thesis. For a detailed description, please refer to the original publications.

3.2.3. Jordan-Wigner Transformation

Tensor network methods work naturally with spin or boson operators. Due to the anticommutation relations, however, fermionic operators do not fit natively into the framework. To work with (spinful) fermions, we use the Jordan–Wigner transformation that maps between spin- $\frac{1}{2}$ operators and fermionic creation and annihilation operators. These spin- $\frac{1}{2}$ operators can also be interpreted as hard-core boson operators:

$$S_i^+ \leftrightarrow a_i^\dagger, \qquad S_i^- \leftrightarrow a_i \,.$$
 (3.23)

Hard-core bosons are particles that obey bosonic statistics but have an additional constraint preventing them from occupying the same quantum state. They therefore anti-commute like fermions for the same state and commute like bosons for different states. Since we are working with spinful fermionic operators, a second spin- $\frac{1}{2}$ degree of freedom needs to be added:

$$S_{i,\uparrow}^+ \leftrightarrow a_{i,\uparrow}^\dagger, \qquad S_{i,\downarrow}^+ \leftrightarrow a_{i,\downarrow}^\dagger.$$
 (3.24)

We can now define the Jordan–Wigner transformation to map spinful fermion operators on spinful boson operators [104]:

$$\hat{c}_{i,\uparrow} = \hat{F}_1 \hat{F}_2 \cdots \hat{F}_{i-1} \hat{a}_{i,\uparrow}, \tag{3.25}$$

$$\hat{c}_{j,\downarrow} = \hat{F}_1 \hat{F}_2 \cdots \hat{F}_{j-1} (\hat{F}_j \hat{a}_{j,\downarrow}). \tag{3.26}$$

The so-called Jordan-Wigner string operator \hat{F}_j is defined as

$$\hat{F}_j = (1 - 2\hat{n}_{j\uparrow})(1 - 2\hat{n}_{j\downarrow}) = (-1)^{\hat{n}_j}. \tag{3.27}$$

This mapping ensures the correct fermionic anticommutation (2.9) for operators acting on different sites. Note that this transformation maps \hat{c}_j , \hat{c}_j^{\dagger} to global operators. However, most of these non-local parts usually cancel. For example, the Hubbard Hamiltonian (2.18) maps to

$$\hat{H} = -t_h \sum_{j} \left((\hat{a}_{j,\uparrow}^{\dagger} \hat{F}_j) \hat{a}_{j+1,\uparrow} - (\hat{a}_{j,\uparrow} \hat{F}_j) \hat{a}_{j+1,\uparrow} + (\hat{a}_{j,\downarrow}^{\dagger} \hat{F}_{j+1}) \hat{a}_{j+1,\downarrow} - (\hat{a}_{j,\downarrow} \hat{F}_{j+1}) \hat{a}_{j+1,\downarrow} \right) + \hat{H}_U. \quad (3.28)$$

3.3. Finite-Entanglement Scaling

Quantum critical systems exhibit long-range correlations characterized by a diverging correlation length and increasing entanglement. Since iMPS can only capture systems with finite entanglement, their accuracy for critical systems is limited by the finite bond dimension χ . Similar to the well established finite-size scaling, utilized to account for universal behaviours in finite-size systems, finite-entanglement scaling leverages the universal nature of errors induced by finite entanglement.

One way to describe critical phenomena in 1+1 dimensions is through conformal field theory (CFT). With its help, it has been shown that in the critical region, where the correlation length is much larger than the lattice spacing ($\xi \gg a$), the entanglement entropy of a large one-dimensional system scales like [88]

$$S_{\chi} \sim \frac{c}{6} \log \xi_{\chi} \,. \tag{3.29}$$

The dimensionless number c is called central charge and uniquely describes the universality class of the critical system [12].

Interestingly, the Hubbard model and other spin- $\frac{1}{2}$ Luttinger liquids cannot be described by a CFT because they are not Lorentz-invariant; their spin and charge velocities, v_{σ} and v_{ρ} , act as two different speeds of light. However each sector by itself is conformally invariant and described by a Virasoro algebra with central charge c = 1 [105]. Since the charge sector is gapped at half-filling with U > 0,

it is not expected to influence the scaling, as it only contributes a constant term to the entanglement entropy. A central charge of c=1 is therefore expected for the CFT describing this critical system [12]. Previous numerical studies also showed that the finite effective correlation length induced by finite entanglement in iMPS scales according to the empirical scaling law [20]

$$\xi_{\chi} \sim \chi^{\kappa},$$
 (3.30)

where κ is determined by the central charge [21]

$$\kappa = \frac{6}{c(\sqrt{12/c} + 1)} \,. \tag{3.31}$$

Combining (3.29) and (3.30) also yields the relation

$$S_{\chi} \sim \frac{c\kappa}{6} \log \chi$$
. (3.32)

4. Results

In this chapter we use the numerical methods and theoretical concepts introduced in the previous chapters to analyze the behaviour of the half-filled Hubbard model under a photoexcitation protocol. We begin with a finite-entanglement scaling analysis of the ground state, which serves as a reference point and as a benchmark for our numerical setup. We then continue with the time evolution of the system under the influence of a photo pulse, studying various physical quantities, including the pair correlation function, double occupancy, entanglement entropy, and correlation length. Finally, we attempt to apply finite-entanglement scaling to the system's post-pulse state.

4.1. Finite-Entanglement Scaling

As a baseline, we compute the central charge of the half-filled Hubbard Model in the Mott insulating phase using the scaling relation (3.29) between the entanglement entropy S_{χ} and correlation length ξ_{χ} . Linear fits are performed using ordinary least squares regression. The reported uncertainties correspond to the standard error of the fit. Figure 4.1 shows the scaling behaviour for ground states at $U/t_h=8$, obtained using both iTEBD and VUMPS for a range of bond dimensions from $\chi=20$ up to $\chi=2500$. The fitted slope of 0.1661 agrees with the theoretical expectation of $\frac{c}{6}$, confirming c=1 for the Luttinger liquid description of the gapless spin sector to a high accuracy. This validates the reliability of our numerical approach.

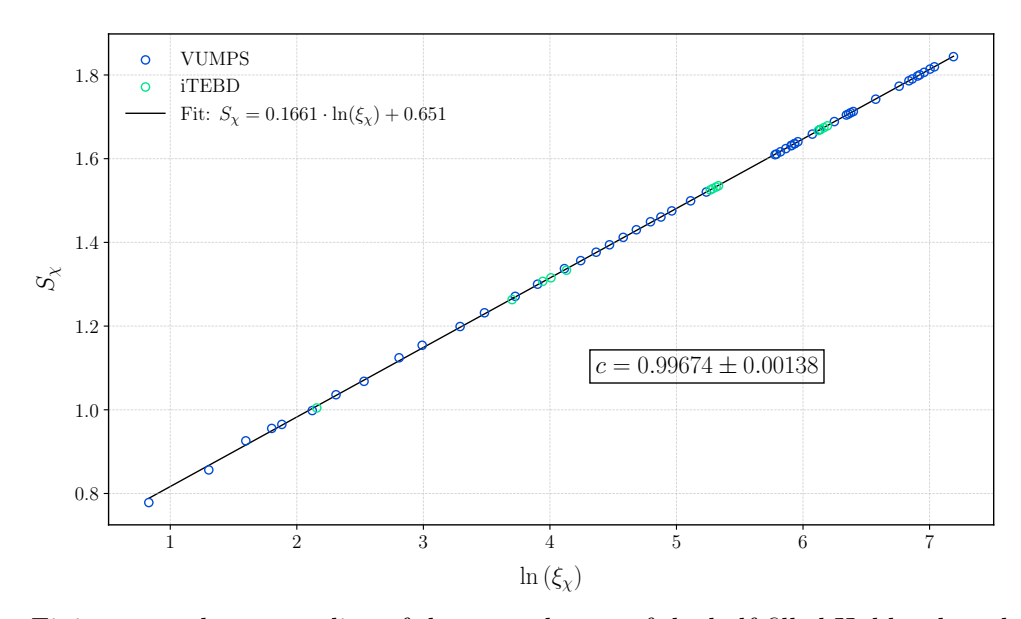


Figure 4.1.: Finite-entanglement scaling of the ground state of the half-filled Hubbard model at $U/t_h=8$. The data shows S_{χ} versus $\log \xi_{\chi}$ for various bond dimensions $20 \le \chi \le 2500$. The linear fit yields a slope close to $\frac{1}{6}$, confirming a central charge of c=1.

If we only consider bond dimensions $\chi \geq 750$, we get an even more accurate result (Fig. 4.2).

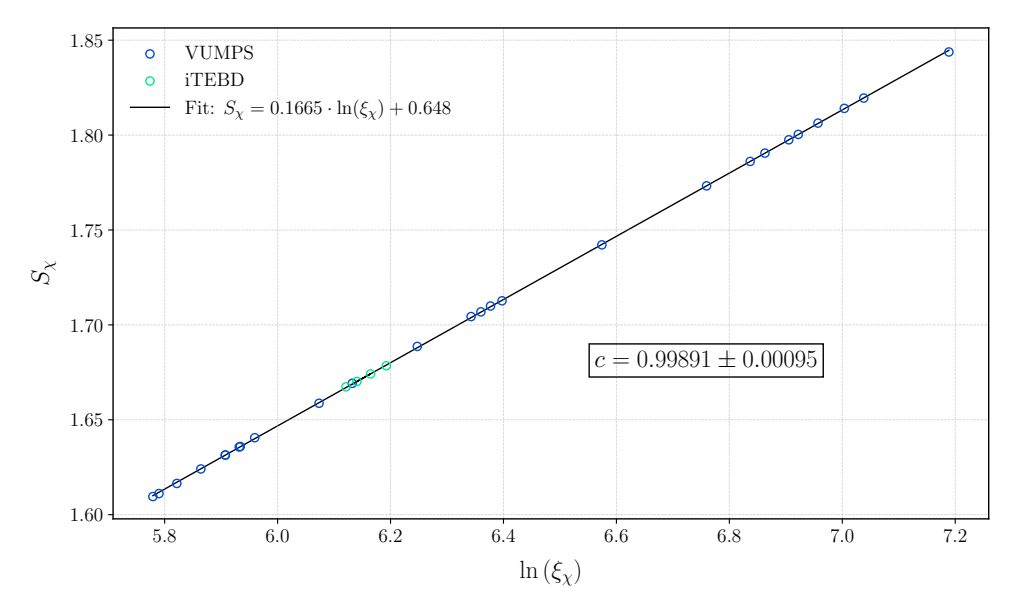


Figure 4.2.: Finite-entanglement scaling of the ground state of the half-filled Hubbard model at $U/t_h = 8$. The data shows S_{χ} versus $\log \xi_{\chi}$ for various bond dimensions $750 \le \chi \le 2500$. The linear fit yields a slope close to $\frac{1}{6}$, confirming a central charge of c = 1.

As an additional benchmark, we also compute the central charge in the non-interacting limit of the Hubbard model $(U/t_h = 0)$. In this regime, the system is equivalent to two decoupled gapless fermionic chains, corresponding to the independent charge and spin sectors, resulting in a central charge of c = 1 + 1 = 2.

Figure 4.3 shows the finite-entanglement scaling of the entanglement entropy with respect to the correlation length for the ground state at $U/t_h=0$, using VUMPS. The fitted slope is in agreement with the theoretical prediction $s=\frac{c}{6}=\frac{1}{3}$, confirming c=2.

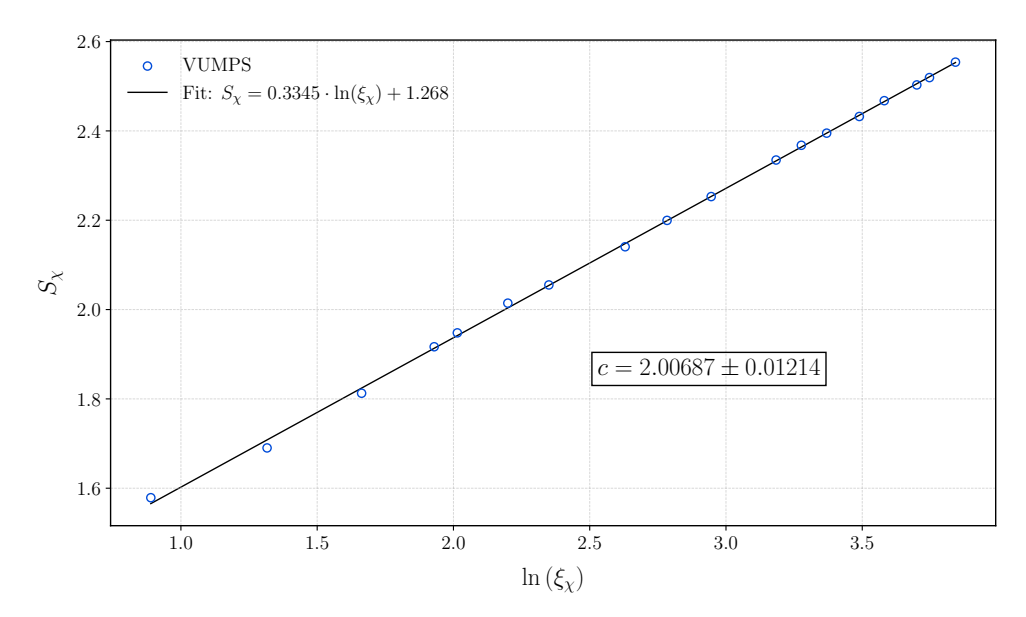


Figure 4.3.: Finite-entanglement scaling of the ground state of the half-filled Hubbard model at $U/t_h = 0$. The data shows S_{χ} versus $\log \xi_{\chi}$ for various bond dimensions $90 \le \chi \le 900$. The linear fit yields a slope close to $\frac{2}{6}$, confirming a central charge of c = 2.

Chapter 4. Results

4.1.1. Scaling with Bond Dimension

While the scaling $\xi \sim \chi^{\kappa}$ and consequently $S_{\chi} \sim \frac{c\kappa}{6} \log \chi$ was qualitatively observed (see Fig. 4.4), the extracted exponent κ shows systematic deviations from the theoretical prediction (3.31). These deviations are present both at $U/t_h = 0$ (c = 2) and $U/t_h = 8$ (c = 1), and interestingly, they become more pronounced at larger bond dimensions χ . The derivation of κ by Pollmann et al. assumes a critical point separating two gapped phases, which can be described by a single CFT. These assumption do not perfectly fit the Hubbard model: At $U/t_h = 0$, it is a Luttinger liquid with two decoupled c = 1 sectors, each described by a CFT. The truncation of entanglement in iMPS acts independently on each sector, which could affect the scaling behaviour. At $U/t_h = 8$, the model is in a critical phase rather than at a critical point separating two gapped phases.

However, we observed similar deviations for the critical XX model (c=1) [106], which nominally fits Pollmann's assumptions, using both the iTEBD and VUMPS algorithms. Figure 4.4 presents these deviations for all three models; a comprehensive summary of results for different models, parameters, and bond dimensions is provided in Appendix A.

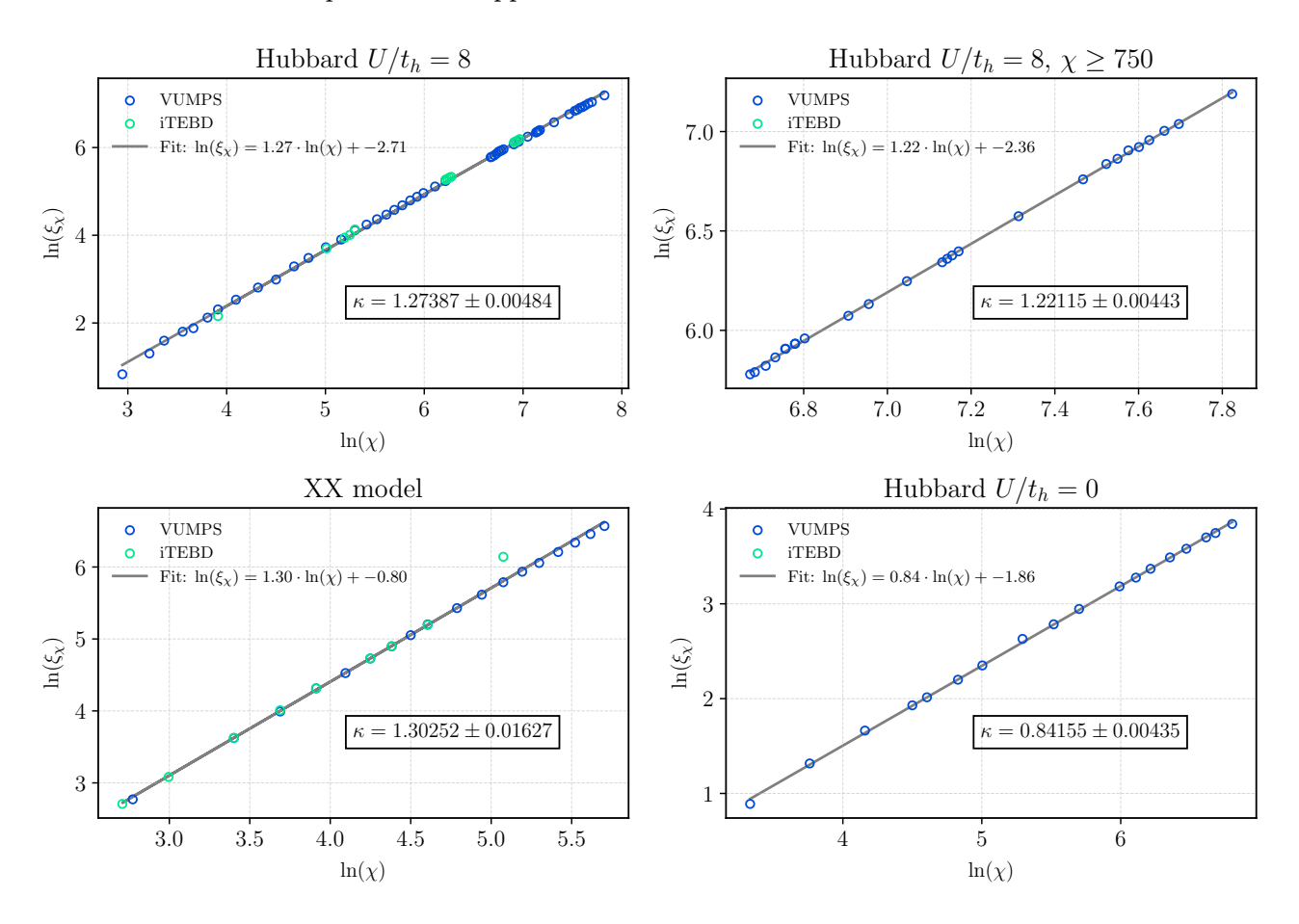


Figure 4.4.: Finite-entanglement scaling for various models, algorithms, parameters and bond dimension ranges. The linear fits confirm the $\xi_{\chi} \sim \xi^{\kappa}$ scaling relation with a Pearson correlation coefficient R > 0.999. The extracted exponent κ , however, does not confirm the theoretical prediction (3.31) of $\kappa_{\rm th} = 1.344055$ for c = 1 and $\kappa_{\rm th} = 0.869694$ for c = 2. The deviation seems to increase for larger bond dimensions χ .

To fully understand the origin of these deviations, a more detailed study would be required. However, since this is not the main focus of the present work, it is not explored further here.

4.2. Photoinduced Dynamics

We now turn to the effect of a photo pulse on the Mott insulating phase of the half-filled Hubbard chain at $U/t_h = 8$. Starting from the ground state obtained using VUMPS at time t = 0, we add the time-dependent external field (2.40) modeling a pump pulse as discussed in section 2.4.1. The system is driven out of equilibrium as $|\psi(0)\rangle \rightarrow |\psi(t)\rangle$, with its time evolution simulated using the iTEBD algorithm with a time step $\tau = 0.0025$ if not stated otherwise. All simulations are performed with a two-site unit cell. For comparison, we also tested a four-site unit cell at lower bond dimensions but found no differences. We use a pulse tuned to parameters that were previously identified as optimal for inducing maximal η -pairing correlations in the half-filled Hubbard model [15, 107]. It is centered at time $t_0 = 10$, with a width of $\sigma_p = 2$, an amplitude $A_0 = 0.37$ and a frequency of $\omega_p/t_h = 7.1$. These values correspond to the pulse shown in Fig. 2.1. Additionally, we also consider parameters that maximize the double occupancy. This is achieved with amplitude $A_0 = 0.95$ and frequency $\omega_p/t_h = 8.4$. The centering and width is the same as for the η -pairing-dominant pulse. Following the pulse, the system is expected to undergo a pronounced change in dynamical behaviour, providing a concrete example of how targeted out-of-equilibrium protocols can generate nontrivial quantum states that cannot be captured by traditional equilibrium statistical mechanics.

4.2.1. η -Pairing

Figure 4.5 shows a significant enhancement of the double occupancy, $P(r=0,t)=2n_d(t)$, during both pulses. Due to its local character, the double occupation is captured accurately even at lower bond dimensions and plateaus almost independently of χ after the pulse. However, it remains slightly more stable for higher bond dimensions. As expected, the double-occupancy-dominant pulse plateaus at a higher value and, interestingly, exhibits a high peak before the center of the pulse. The double occupancy following both pulses shows a minor peak at $t \approx 12.5$ and subsequently reaches a minimum at $t \approx 15$, after which it remains constant. This confirms the results of Ref. [15] and shows that the increased double occupancy remains stable for longer periods.

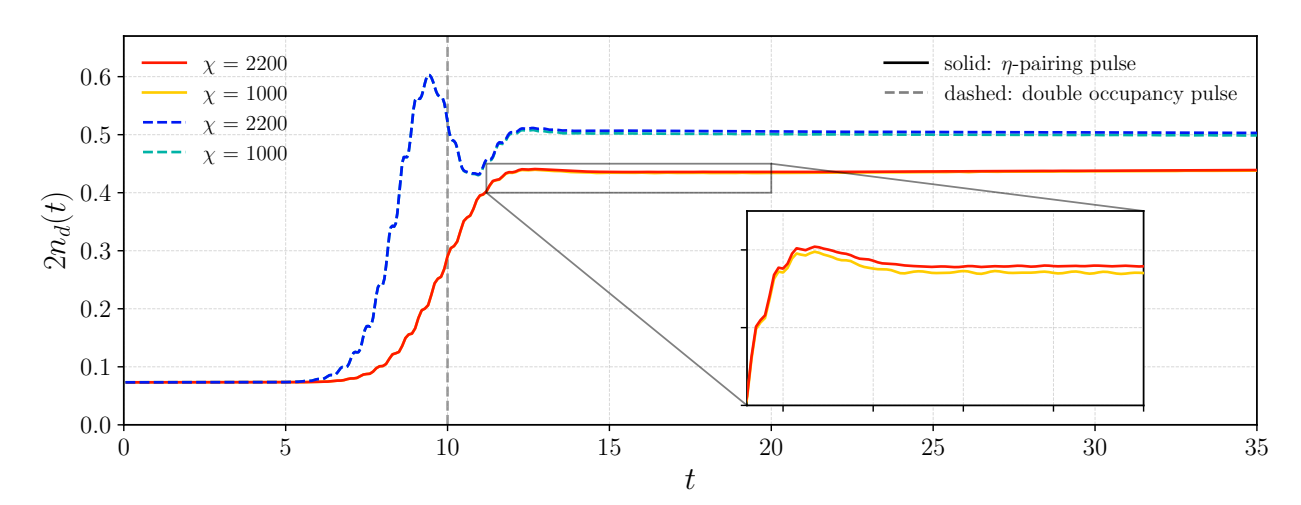


Figure 4.5.: Time evolution of the double occupancy for various bond dimensions χ . Solid lines represent the η -pairing-dominant pulse, while dashed lines denote the double-occupancy-dominant pulse. The vertical dashed line marks the center of the pulses.

As shown in Fig. 4.6, $P(r \neq 0, t)$ also exhibits a considerable increase during the pulse for both pulse types. P(r,t) alternates in sign between odd and even distances r, which is typical for η -pairing states [14]. These longer-ranged correlations are induced by the photo pulse and are absent in the

28 Chapter 4. Results

Mott insulating ground state at t=0 (see Fig. 4.7). For the pulse maximizing double occupancy, this induced correlation decays quickly after the pulse ends, returning close to its initial value within $t\approx 25$. In contrast, for the η -pair-maximizing pulse, the increased correlations remain stable throughout the simulation, indicating the formation of a robust η -pairing state. We found that it is important to use a sufficiently small time step τ , as larger values induce an unphysical drift in the pair correlations over time.

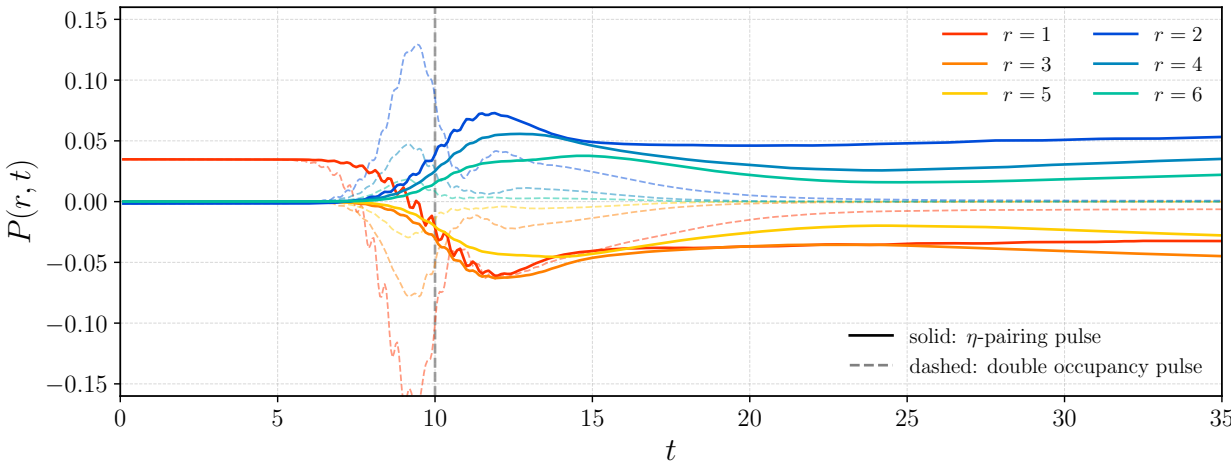


Figure 4.6.: Time evolution of the pair correlation function P(r,t) for different distances r. Solid lines represent the η -pairing-dominant pulse, while dashed lines denote the double-occupancy-dominant pulse. The vertical dashed line marks the center of the pulses. Simulations were performed using $\chi=2200$.

Figure 4.7 also shows that the pair correlations, which are initially localized at short distances, appear to spread outward following the photoexcitation. Specifically, we observe that the short-range pair correlations decrease over time, while correlations at longer distances grow. This suggests an outward propagation of pairing correlations following the photoexcitation. Such behaviour is reminiscent of the light-cone effect observed after quenches [108–110], where correlations spread at a finite velocity determined by the underlying quasiparticle dynamics. In this picture, the pulse acts as a source of quasiparticles. Figure 4.8 further illustrates this effect, showing that the pair correlations spread with an approximately constant velocity after the pulse.

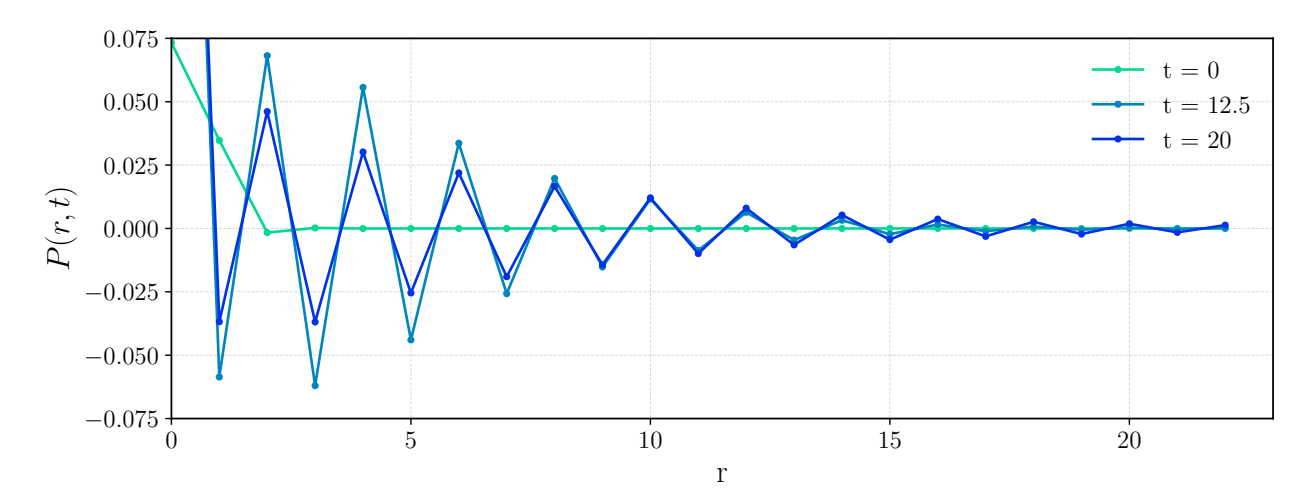


Figure 4.7.: Pair correlation function at times t = 0 (ground state), t = 12.5 and t = 20. The results were obtained using a bond dimension of $\chi = 2200$.

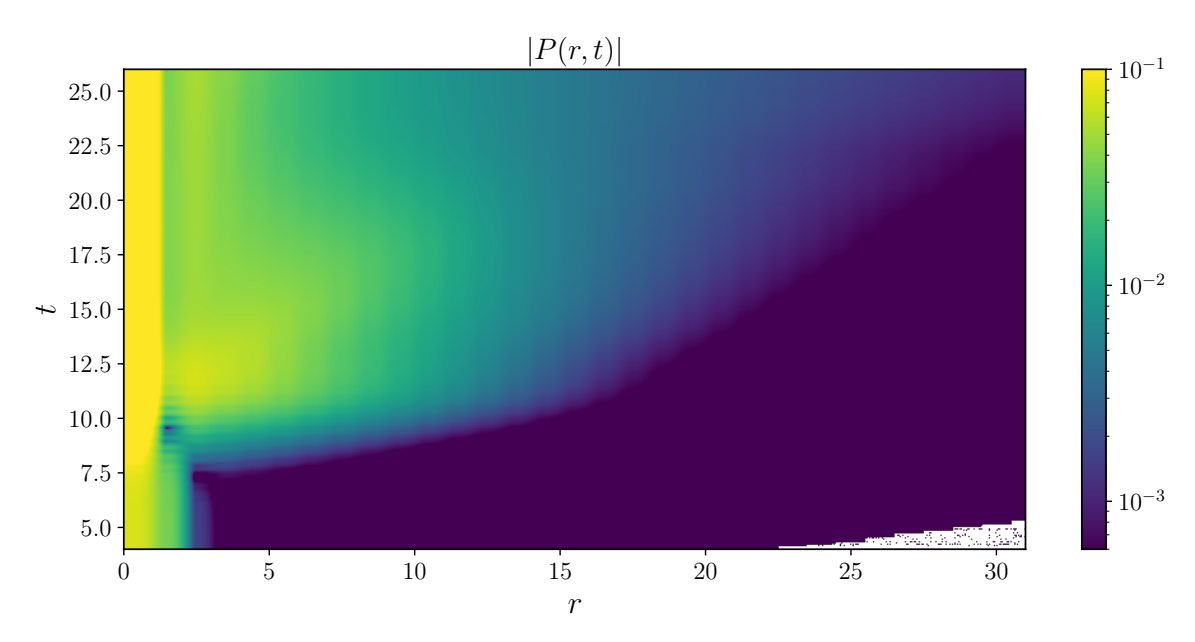


Figure 4.8.: Heatmap of the absolute value of the pair correlation function |P(r,t)|. The results show the outward spreading of pair correlations over time, indicative of a finite-velocity propagation front following the photoexcitation. Computed with bond dimension $\chi = 2200$.

The qualitative features of P(r,t) are consistent across various bond dimensions. The decrease as a function of r can be attributed to the limitations of the iMPS representation, which can only approximate the expected long-range correlations as a sum of exponentials. Figure 4.9 illustrates the dependence of P(r,t) on bond dimension χ . Even a relatively large bond dimension, such as $\chi=2499$, still significantly limits the amount of long-range correlations that can be captured by the iMPS ansatz. This constraint becomes increasingly pronounced at larger distances r. While previous finite-size studies for this pulse protocol demonstrated the discrepancy between exact diagonalization and the MPS method (see Ref. [14] and its supplementary material), the infinite MPS appears to face even greater challenges in accurately capturing long-range correlations, especially at large distances.

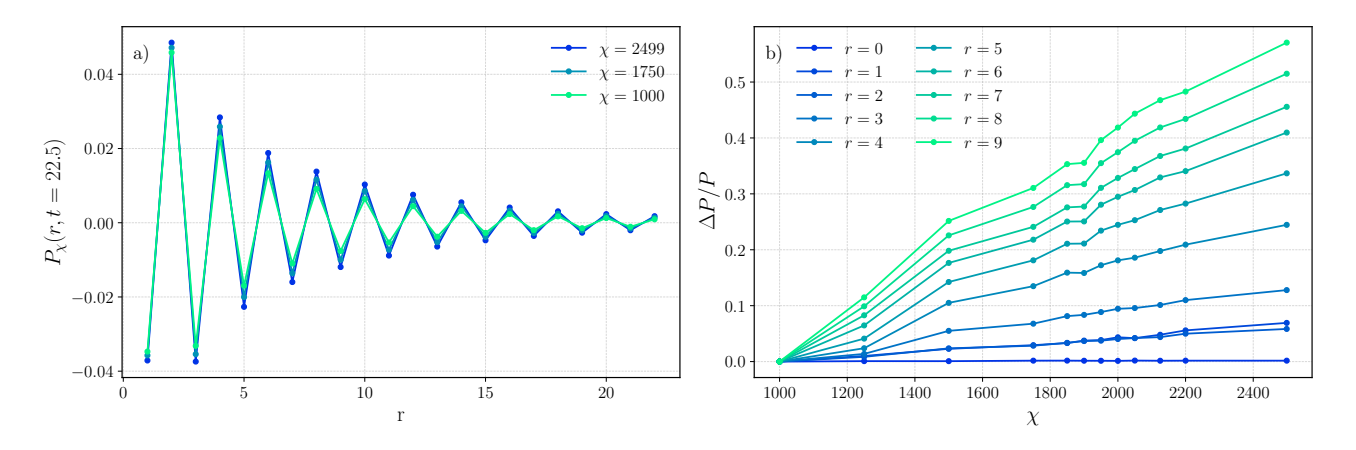


Figure 4.9.: (a) Pair correlation function $P_{\chi}(r,t)$ at fixed time t=22.5 for different bond dimensions χ . Increasing the bond dimension leads to higher values of the pair correlation. (b) Relative difference $\Delta P/P = [P_{\chi}(r,t=22.5) - P_{1000}(r,t=22.5)]/[P_{1000}(r,t=22.5)]$ of P_{χ} to P_{1000} at t=22.5. The relative difference increases as χ increases and grows faster at larger r. The iTEBD simulations were performed using $\tau=0.005$.

30 Chapter 4. Results

The Fourier transform $\widetilde{P}(q,t)$ (also called the pair structure factor), shows a clear peak at $q=\pi$ after the pulse, as expected from the alternating sign. Figure 4.10 demonstrates the enhancement of $\widetilde{P}(\pi,t)$ during the pulse, which strongly indicates the emergence of η -pairing in the system. These results are consistent with previous findings [15]. For finite systems, further evidence of η -pairing is provided in Ref. [14], where the overlap wit η -pairing eigenstates is explicitly computed.

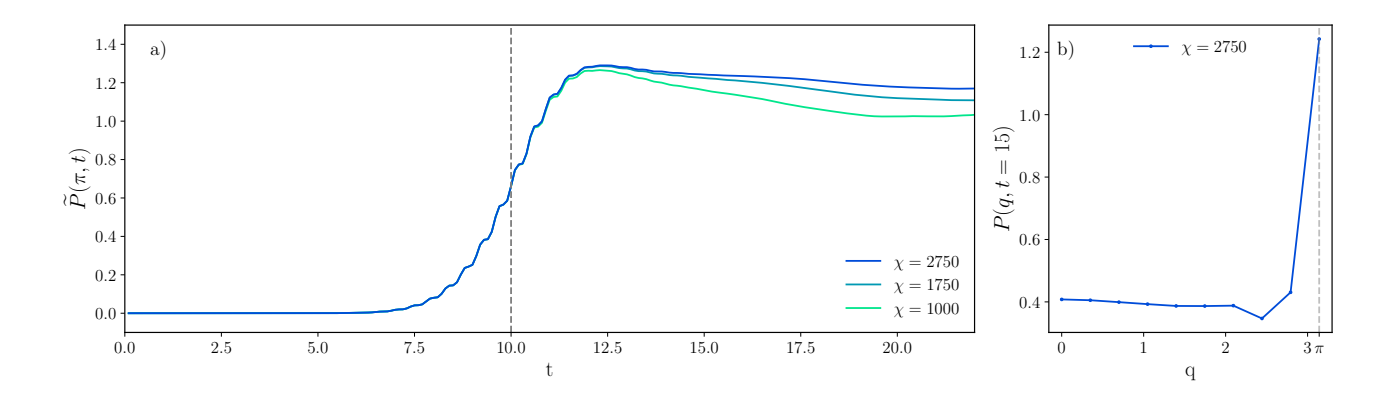


Figure 4.10.: (a) Time evolution of $\widetilde{P}(\pi,t)$ for different bond dimensions χ with $\tau=0.005$. The Fourier transform was computed using P(r,t) up to a range of r=128. $\widetilde{P}(\pi,t)$ plateaus at a value dependent on χ . The decrease is due to numerical errors as it should be constant due to the commutation relation (2.28). (b) Peak of the pair structure factor at $q=\pi$.

4.2.2. Dynamical Quantum Phase Transitions

Having established that the photoexcited state exhibits properties that are absent in any region of the ground-state phase diagram, we now investigate whether these changes are accompanied by a DQPT. It is important to emphasize again that this scenario differs qualitatively from most other DQPT studies, which typically involve sudden quenches or slow ramps. Although DQPTs have been investigated in Floquet systems [68, 69], to the best of our knowledge, they have not yet been studied within photo-pulse protocols.

Quench Protocol

Before we inspect this novel scenario, we first demonstrate a prototypical DQPT in a sudden quench. Specifically, we cross the metal-insulator transition of the half-filled Hubbard model by starting in the non-interacting ground state with $U_0 = 0$, and then suddenly turning on interactions to U > 0 at time t = 0 while keeping $t_h = 1$ constant.

For a two-site system and assuming $U \gg 1$, strong-coupling time-dependent perturbation theory [111] can be used to time-evolve the known ground state

$$|\psi_0\rangle = \frac{1}{2} (|\uparrow\downarrow,0\rangle + |\uparrow,\downarrow\rangle - |\downarrow,\uparrow\rangle + |0,\uparrow\downarrow\rangle) \tag{4.1}$$

as [112]

$$|\psi(t)\rangle = e^{-i\hat{H}_U t} |\psi_0\rangle + \frac{2t_h}{U} (1 - e^{-iUt}) |\psi_0\rangle. \tag{4.2}$$

Now the Loschmidt echo is easily obtained as

$$\mathcal{L}(t) = \cos^2\left(\frac{Ut}{2}\right) + \frac{16}{U^2}\sin^2\left(\frac{Ut}{2}\right). \tag{4.3}$$

Calculating other quantities, such as $\langle S_i^z(t)^2 \rangle$ and the double occupancy $n_d(t)$, reveals that they all oscillate with a period of $\frac{2\pi}{U}$. In the context of DQPTs, however, it is immediately apparent that the Loschmidt echo is continuous and exhibits no non-analyticities. This is because Fisher zeros in the complex time plane only accumulate as the system size increases [18], leading to DQPTs in the thermodynamic limit.

Figure 4.11 shows the results of our simulations in the thermodynamic limit using iTEBD. DQPTs emerge periodically and appear earlier and more frequently for larger U, closely resembling the periodicity of the Loschmidt echo (4.3) in the two-site system.

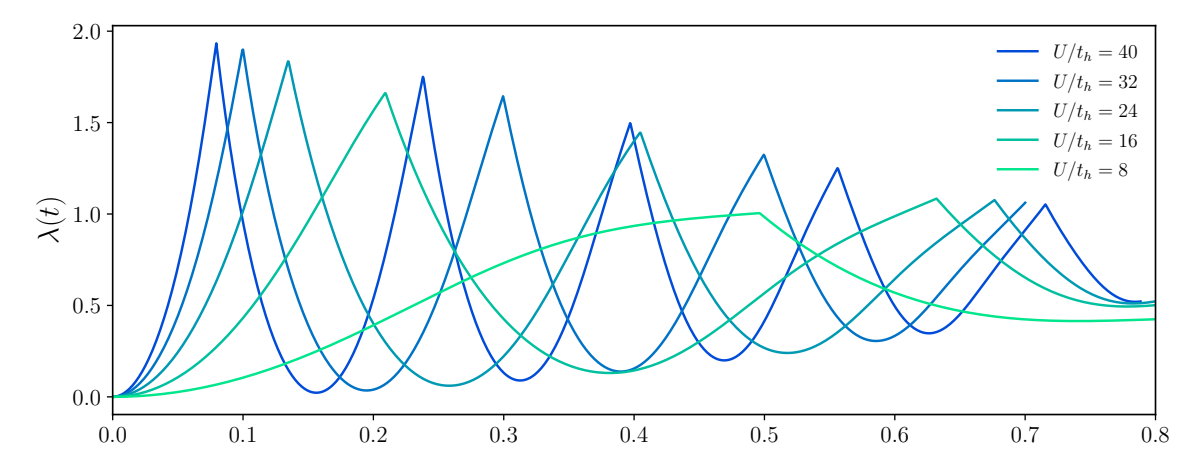


Figure 4.11.: Rate function $\lambda(t)$ following quenches from $U_0 = 0$ to various finite U in the half-filled Hubbard model. Pronounced cusps are visible, signaling DQPTs. The calculations were carried out using $\chi = 900$ and $\tau = 0.0005$.

32 Chapter 4. Results

The agreement between our simulation and the two-site prediction improves with increasing U as expected from the strong-coupling perturbation theory approximation. For $U \gtrsim 32$, the cusps almost perfectly coincide with the predicted minima of the Loschmidt echo (4.3) (maxima of the corresponding rate function) in the two-site system. For U=48, the agreement is perfect within the limits of our time step resolution. The same holds for the maxima of $\langle S_i^z(t)^2 \rangle$ and the minima of $n_d(t)$, as demonstrated in Fig. 4.12. In this regime, spin dynamics, charge dynamics, and DQPTs evolve on the same timescale. However, in the infinite system, the oscillations are damped.

Our results closely reproduce earlier studies [112] which showed that DQPTs already appear in large but finite systems. Our calculations, however, achieve even higher accuracy.

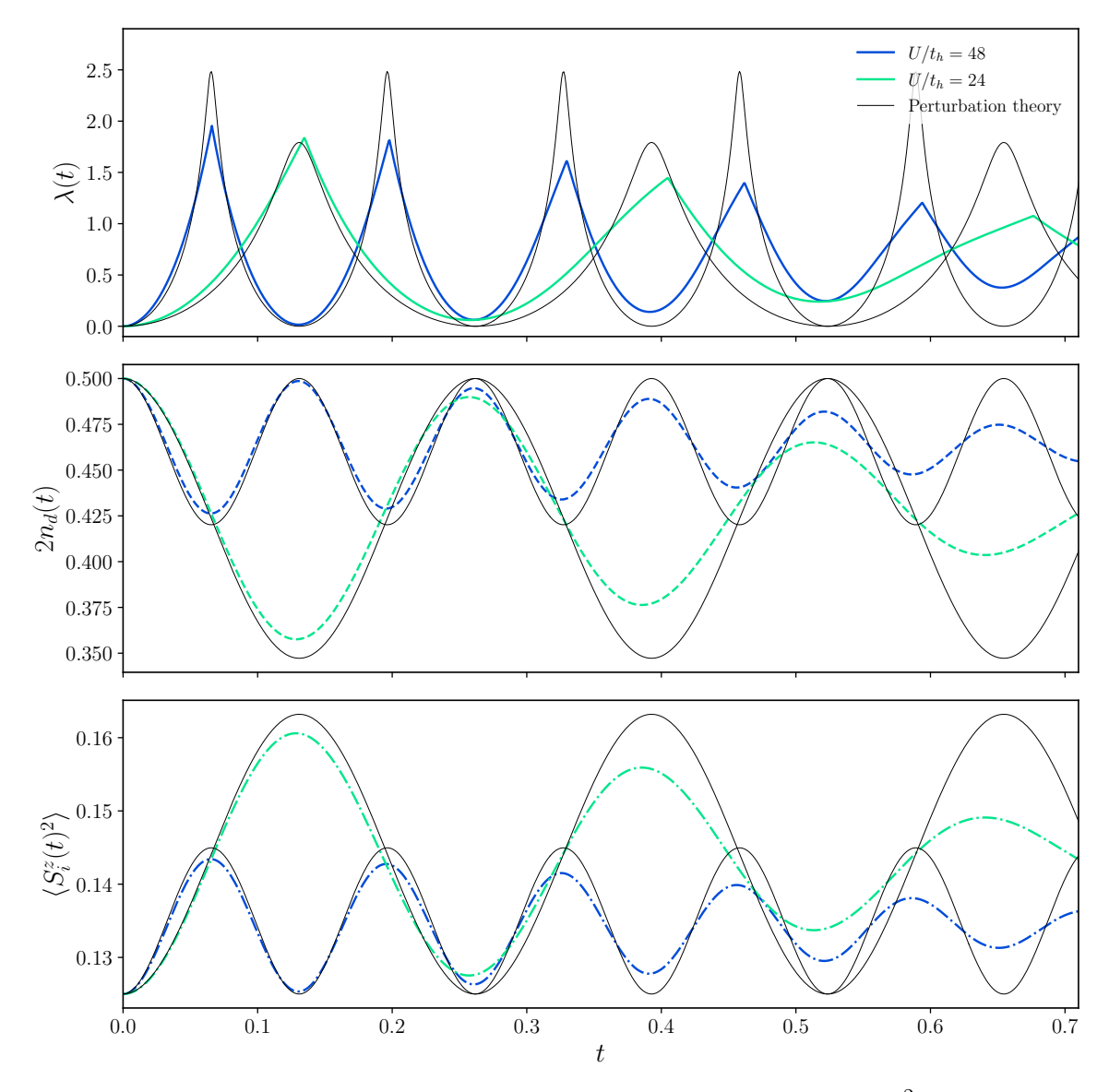


Figure 4.12.: Rate function $\lambda(t)$, twice the double occupancy $2n_d(t)$, and $\langle S_i^z(t)^2 \rangle$ following a quench from $U_0 = 0$ to U = 24 and U = 48 in the half-filled Hubbard model. Agreement with the perturbation theory results for a two-site system, depicted by the thin black lines, increases with U. Clear cusps signaling DQPTs emerge in the otherwise smooth rate function for finite systems. The calculations were carried out using $\chi = 900$ and $\tau = 0.0005$.

Photoinduced Hubbard Model

Having established the classical case, we now turn to the photoexcited case. After the η -pairing-dominant pulse, we observe a non-analytic point at $t_c \approx 15$. The cusps's occurrence immediately after the pulse suggests that the system undergoes a DQPT induced by the photo pulse. As shown in Fig. 4.13, the cusp only shows up at large bond dimensions χ . However, if χ is large enough, the point is consistent across multiple different χ and becomes more pronounced the larger the bond dimension gets. The time t_c roughly coincides with the point at which the double occupancy reaches its minimum. This is similar to the behaviour after the quench, which is further evidence of there being a DQPT even though the cusps are not as sharp as the ones following the quench. A second kink that is only recognizably for $\chi \geq 2200$ occurs at $t_c \approx 20$ signaling another DQPT similar to the recurring DQPTs in the quench case. Beyond this point, numerical errors begin to dominate and further conclusions cannot be drawn.

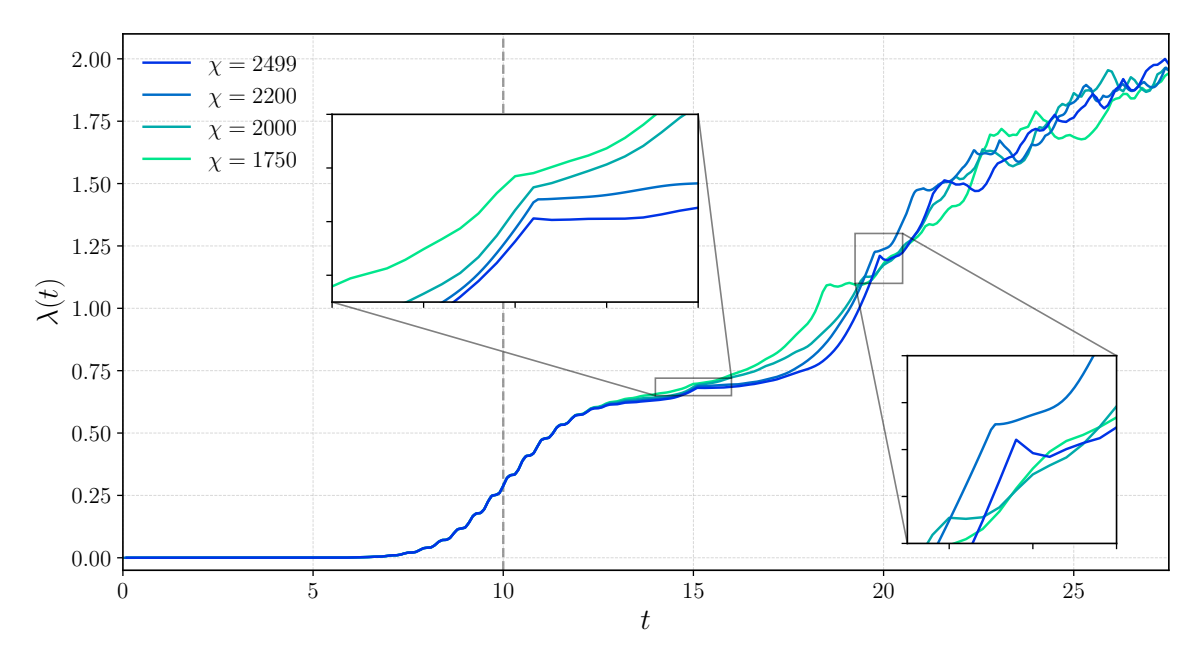


Figure 4.13.: Loschmidt echo rate function during the η -pairing-dominant pulse for different bond dimensions χ . The iTEBD simulations were run using a time step of $\tau = 0.0025$. The insets highlight non-analytic points after the pulse.

Figure 4.14 shows that the Trotter error plays a large role in these numerical instabilities at longer times, as the second cusp becomes really pronounced even for $\chi=2200$ if the time step is small enough. The rate function also stays smooth for longer times if the time step is smaller.

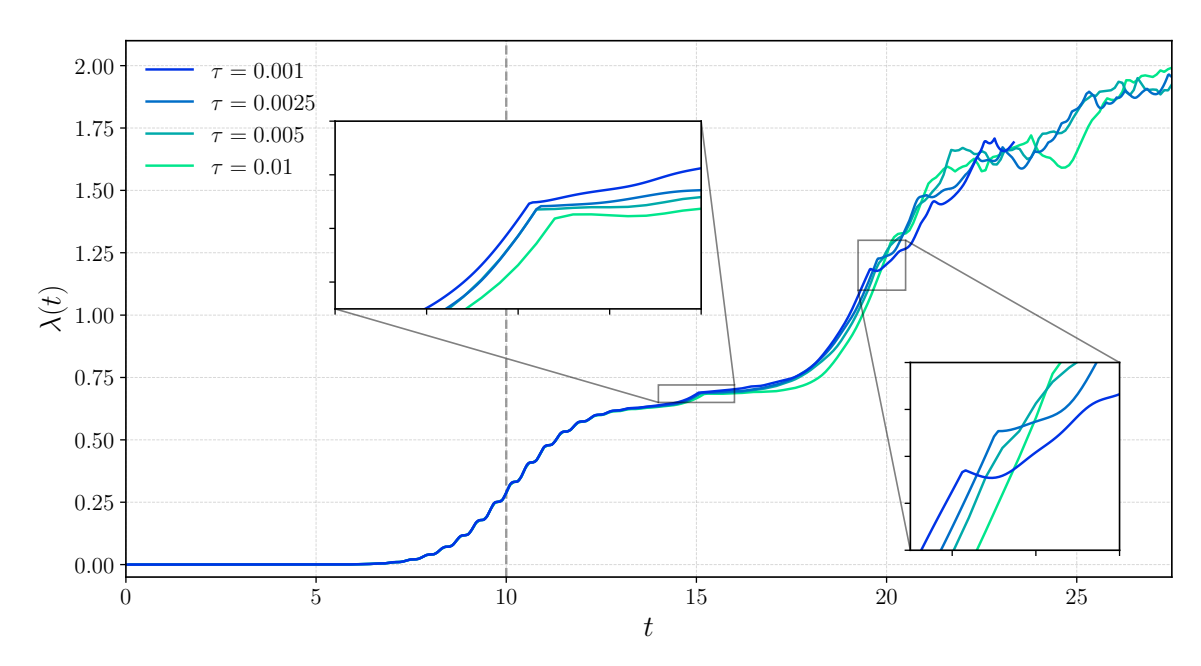


Figure 4.14.: Loschmidt echo rate function during the η -pairing-dominant pulse for different time steps τ at a fixed bond dimension $\chi = 2200$.

For the double-occupancy-dominant pulse, the rate function exhibits a smooth peak shortly before the center of the pulse, closely mirroring the behaviour observed in the double occupancy. The rate function displays some cusps at $t\approx 15$ and at later times (see Fig. 4.15). However, these features show little consistency across different bond dimensions, indicating significant numerical uncertainty. Therefore, a clear identification of a DQPT is not possible based on the current data. One interesting feature to note is that the rate function levels off much earlier than that of the η -pairing pulse, indicating a more stable state.

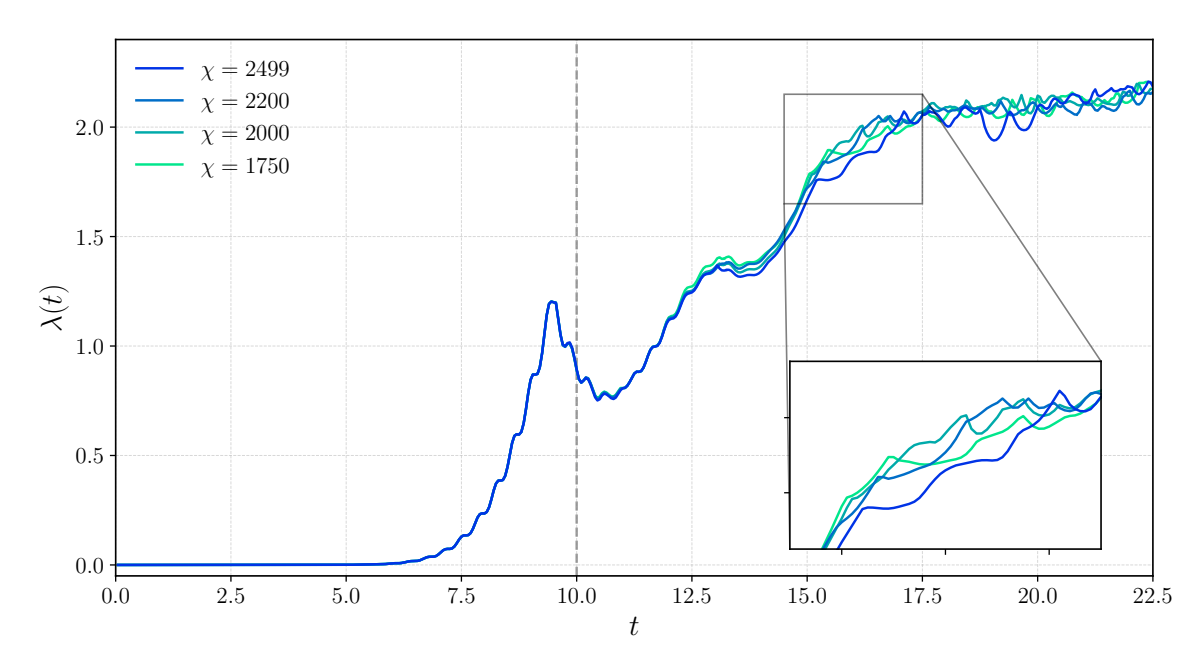


Figure 4.15.: Loschmidt echo rate function during the double-occupancy-dominant pulse for different bond dimensions χ . No DQPT can be identified. The iTEBD simulations were run using a time step of $\tau=0.005$.

4.2.3. Entanglement Entropy, Correlation Length, and Finite-Entanglement Scaling Entanglement Entropy

As can be seen in Fig. 4.16, the von Neumann entanglement entropy increases linearly during both pulses and shortly afterwards.

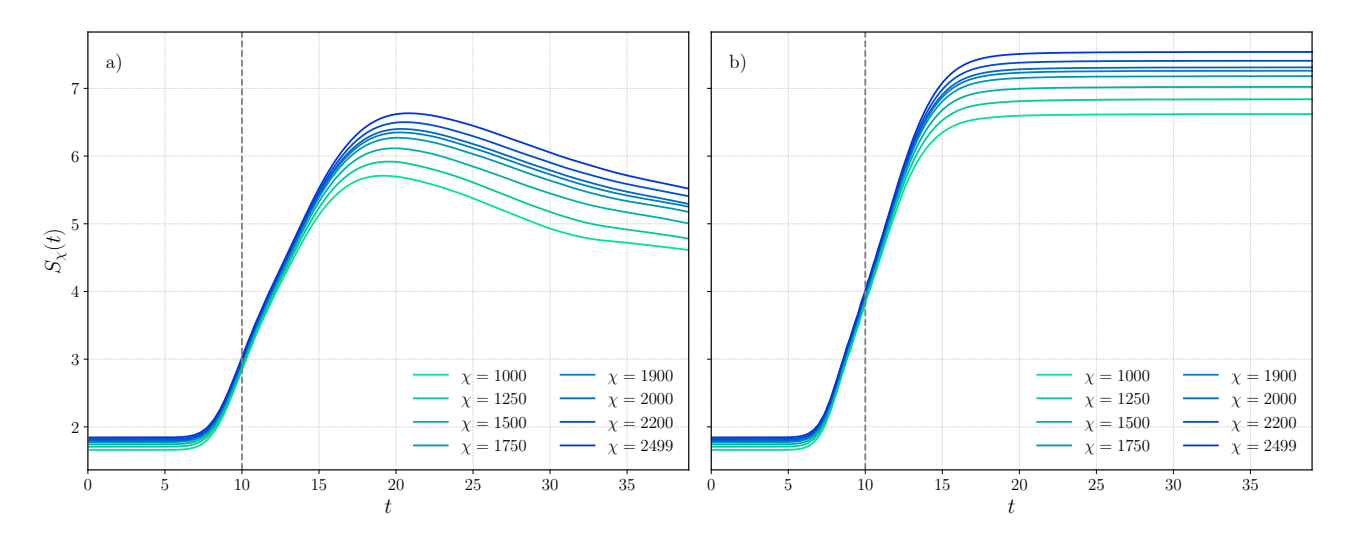


Figure 4.16.: Time evolution of the von Neumann entanglement entropy for different bond dimensions χ using (a) the η -pairing-dominant pulse and (b) the double-occupancy-dominant pulse. Simulations were performed using $\tau = 0.005$.

The increase in entanglement entropy reflects the departure from equilibrium, the creation of a highly entangled excited state, and can be related to the induced correlations. For the η -pairing-dominant pulse, the entanglement entropy S_{χ} stops increasing around $t\approx 17$ and then begins to decrease again at approximately $t\approx 20$. This decrease of entanglement entropy is likely a numerical error, as using smaller time steps resulted in a less pronounced decrease. These observations indicate that the true entanglement and correlations in the system can no longer be represented by the numerics once the bond dimension limit is reached. Any further features such as the drop in entropy should therefore not be interpreted as a genuine property of the system.

In contrast, for the double-occupancy-dominant pulse, which induces fewer long-range correlations, the entanglement entropy grows faster, plateaus and remains stable even at longer times. This indicates that the corresponding state is easier to represent by iMPS and does not push the representation to its limits. These results for the entanglement entropy are consistent with Ref. [107].

Similar entanglement growth has been observed in finite systems under quench protocols. In such settings, entanglement grows linearly in time until it saturates to a value proportional to the subsystem size [113, 114].

Correlation Length

Figure 4.17 displays the time evolution of the correlation length ξ_{χ} for the η -pairing-dominant pulse. Before the pulse, it is stable and shows the expected scaling behaviour. During the pulse, the correlation length drops sharply and the values for different bond dimensions converge. This indicates that the spin sector becomes non-critical, with a finite intrinsic correlation length ξ_0 independent of χ . Figure 4.18 explicitly shows that the antiferromagnetic spin correlations present in the ground state vanish during the pulse, and further analysis of the spin correlation function reveals that it transitions from algebraic to exponential decay. Physically, the pulse injects energy to create η pairs, pushing the system into a transient regime dominated by η -pairing correlations rather than critical spin waves. Because the iMPS representation is not able to capture the long-range correlations, the correlation length does not diverge.

The inset in Fig. 4.17 shows that after the pulse, there is a kink around $t \approx 17$, after which the correlation length slightly increases again and the results for different bond dimensions diverge without any uniform scaling behaviour. As we will show shortly, the finite-entanglement scaling breaks down at exactly that point, supporting its interpretation as a transition point marking the end of criticality in the spin sector. Since the kink coincides approximately with the time at which the entanglement entropy stops increasing (see Fig. 4.16), a formal similarity can also be drawn to the non-analytic features that can appear in correlation function safter quenches in finite systems [108, 115]. These features can emerge at such transition points due to the light-cone-like spreading of correlations and entanglement.

However, the kink could also be a numerical artifact that arises because the iMPS reaches the limit of its bond dimension at this point, such that the growth of entanglement entropy is truncated by numerical constraints.

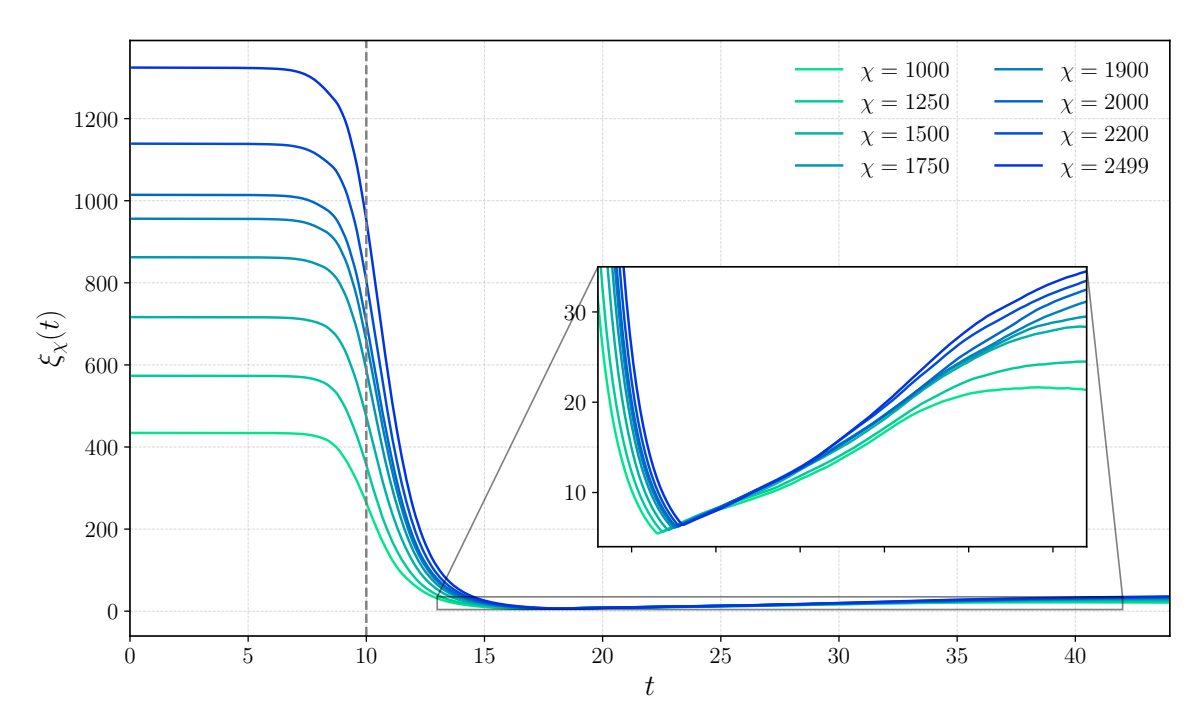


Figure 4.17.: Time evolution of the correlation length ξ_{χ} for different bond dimensions χ during the η -pairing-dominant pulse using $\tau = 0.005$. The correlation length drops sharply during the pulse centered at the dashed vertical line.

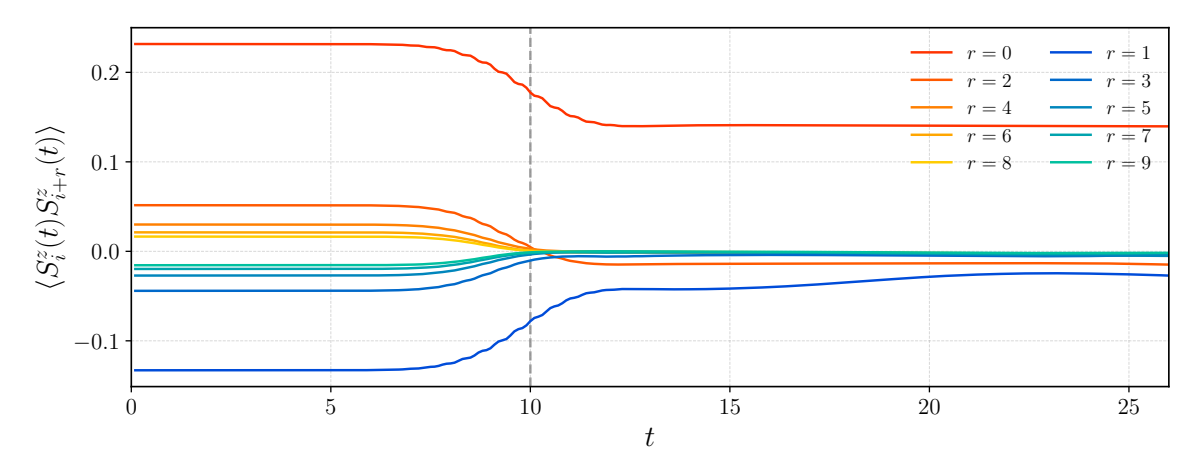


Figure 4.18.: Time evolution of the spin correlation function $\langle S_i^z(t)S_{i+r}^z(t)\rangle$ for different distances r, under the η -pairing-dominant pulse. The vertical dashed line marks the center of the pulses. Simulations were carried out with $\chi=2000$ and $\tau=0.005$.

In case of the more generic, double occupancy-maximizing-pulse, there is a smooth transition instead of a kink, as shown in Fig. 4.19. Other than the smooth turning point, the change in correlation length for the double-occupancy-dominant pulse is qualitatively similar to that of the η -pairing-dominant pulse, indicating a suppression of correlations in the dominant spin sector, similar to what is observed after an η -pairing-dominant pulse. However, the correlation length drops to significantly lower values and exhibits a much smaller increase after the turning point. Thus, a substantial part of the larger correlation length remaining after the η -pairing-dominant pulse can be attributed to the presence of η -pairing correlations, which are absent after the double-occupancy-dominant pulse.

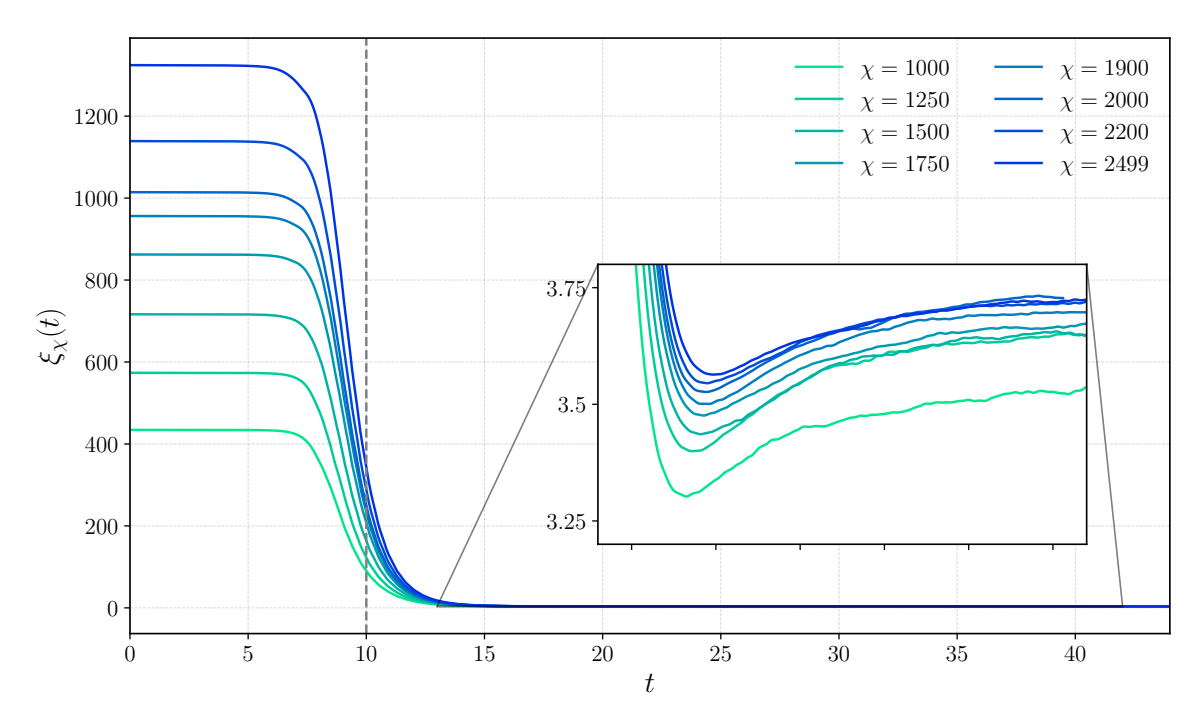


Figure 4.19.: Time evolution of the correlation length ξ_{χ} for different bond dimensions χ during the double-occupancy-dominant pulse using $\tau = 0.005$. The correlation length drops to much lower values than after the η -pairing-dominant pulse.

Finite-Entanglement Scaling

As can be seen from the results in the previous section, both scaling laws including the correlation length, $S_{\chi} \sim \frac{c}{6} \log \xi_{\chi}$ and $\xi_{\chi} \sim \chi^{\kappa}$, no longer apply after the pulse. Specifically, they break down at the kink or the turning point. Figure 4.20 demonstrates how attempts to extract a central charge or effective critical exponent from finite entanglement scaling using the correlation length becomes impossible.

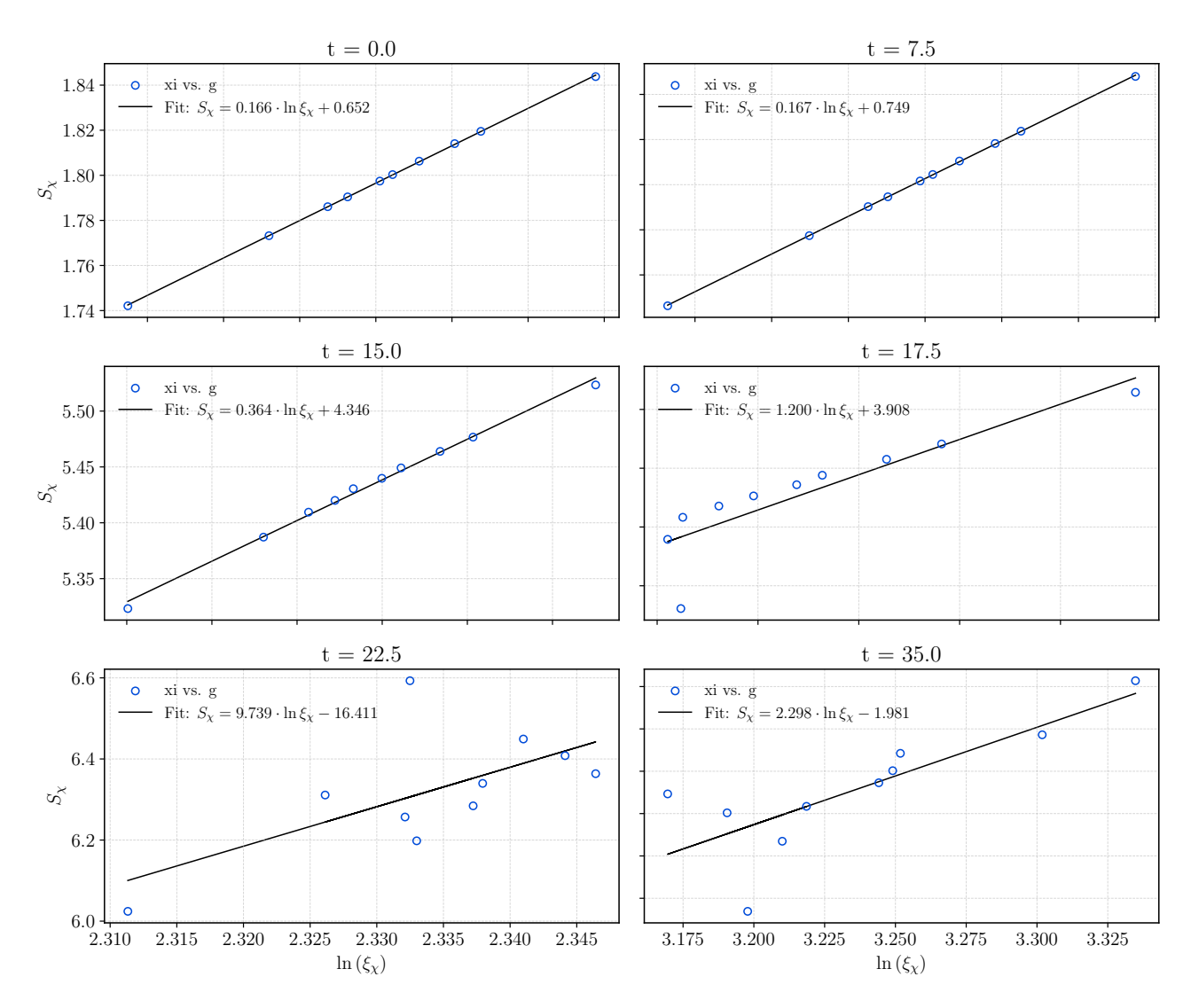


Figure 4.20.: Attempt to fit the scaling relation $S_\chi \sim \frac{c}{6} \log \xi_\chi$ (3.29) before during and after the η -pairing-dominant pulse using $1500 \le \chi \le 2499$. The post-pulse regime does not support the finite-entanglement scaling law. In the observed regime, the correlation length is finite and seems to saturate due to intrinsic physical constraints rather than limitations from the bond dimension. Consequently, attempts to extract a central charge after the pulse yield unphysical or inconsistent results, as the underlying assumptions of the scaling no longer apply.

Interestingly, despite the breakdown of finite-entanglement scaling involving the correlation length, the bond-dimension-based scaling relation $S_{\chi} \sim \frac{c\kappa}{6} \log \chi$ remains valid throughout the entire simulation, as can be seen in Fig 4.16. This scaling behaviour after the η -pairing dominant pulse is demonstrated in Fig. 4.21.

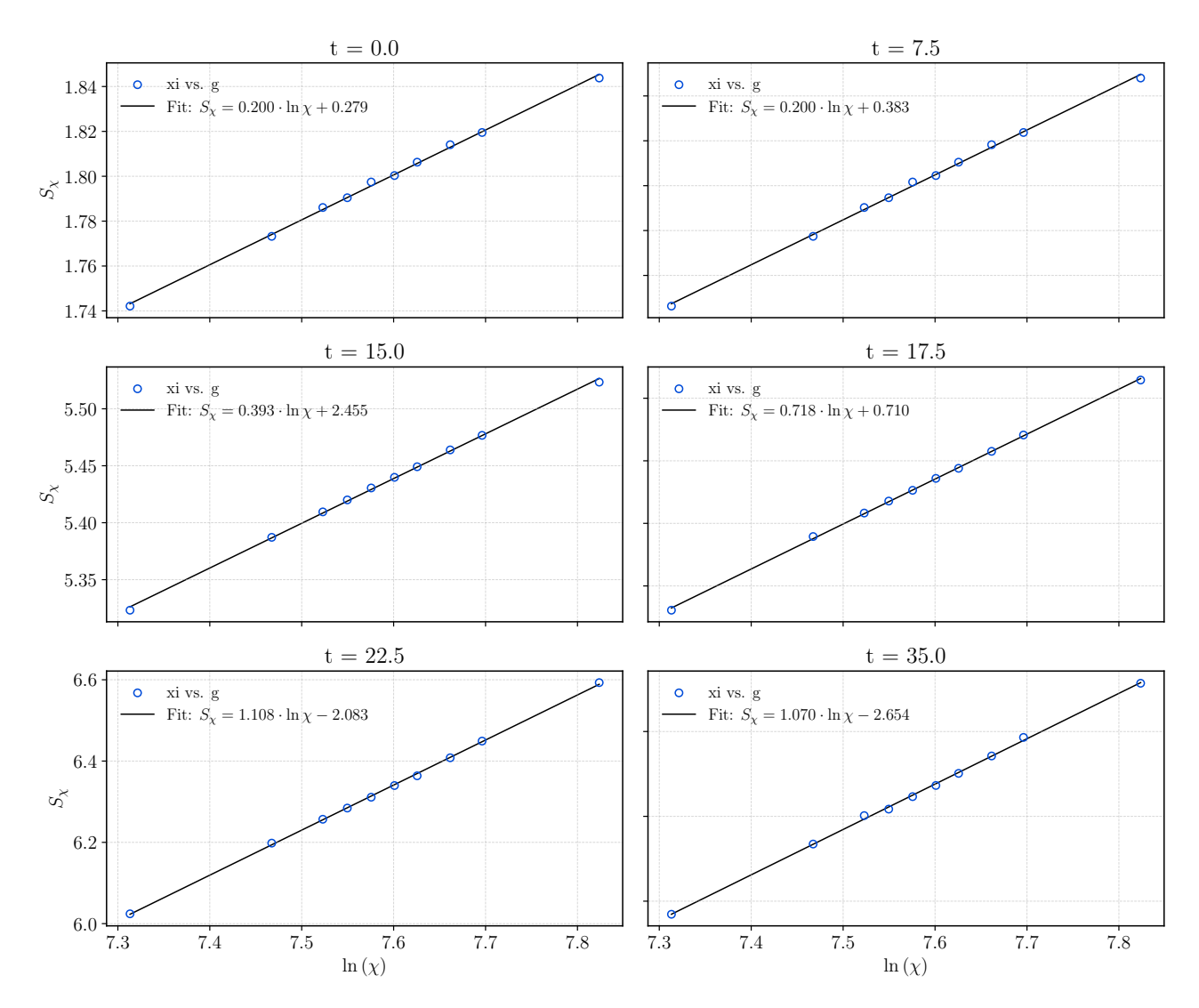


Figure 4.21.: Fit of the scaling relation $S_{\chi} \sim a \log \chi$ (3.32) before during and after the η -pairing-dominant pulse using $1500 \le \chi \le 2499$. The scaling law remains valid during the entire simulation.

This critical-like scaling could be a numerical artifact resulting from the finite bond dimension of the iMPS, which imposes an upper bound of $\log \chi$ on the entanglement entropy. Such a limitation might mimic the scaling seen in critical systems even if the system is in a highly entangled, non-critical state. Figure 4.22 shows the time evolution of the scaling coefficient a extracted from fits to $S_\chi \sim a \log \chi$ for both pulses. The scaling coefficient approaches 1 after the double-occupancy-dominant pulse, showing that the iMPS is nearly saturated and exhibits the maximal entanglement entropy growth possible. The unstable behaviour of the coefficient after the η -pairing-dominant pulse reflects the challenge of correctly capturing the state.

However, we also note a formal similarity to the "hidden criticality" [116] observed in free-fermionic

systems, where entanglement-based measures reveal critical scaling despite the presence of short-range correlations.

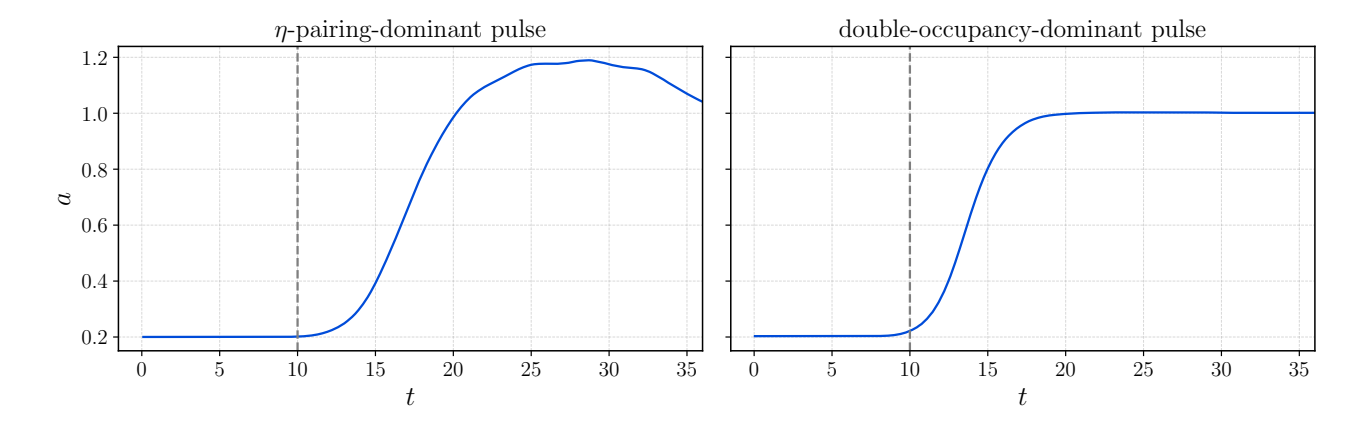


Figure 4.22.: Time evolution of the scaling coefficient a, obtained from fits of $S_\chi \sim a \log \chi$ (as in Fig. 4.21), for both pulses using $1500 \le \chi \le 2499$.

Conclusion and Outlook

We have investigated the real-time non-equilibrium dynamics of the half-filled one-dimensional Hubbard model in the thermodynamic limit using iMPS and the iTEBD algorithm. By simulating photoexcitation through a time-dependent vector potential (Peierls substitution), we explored two central phenomena: the emergence of η -pairing correlations and the occurrence of DQPTs.

Our simulations confirmed that optical pump pulses can induce significant enhancement of the pair structure factor $\widetilde{P}(\pi,t)$, providing numerical evidence for the dynamical generation of η -pairing correlations with ODLRO in a Mott insulator. The persistence of these correlations after optimized pulses suggests the formation of a robust nonthermal state. However, the iMPS representation struggles to correctly represent the highly entangled nature of the excited state due to inherent entanglement bounds.

In addition, we observed non-analyticities in the Loschmidt echo rate function, which serve as signatures of DQPTs. Notably, such DQPT features appear not only in traditional quench protocols (across the metal-insulator transition) but also in the photo pulse protocol. The observed DQPT cusps following photoexcitation, though less sharp than after quenches, were robust across bond dimensions and time steps, supporting their physical rather than numerical origin. In combination with the similar entanglement growth pattern as after quenches, this establishes a direct connection between these different non-equilibrium protocols.

Finite-entanglement scaling allowed us to extract the central charge c=1 before the pulse with high accuracy, confirming the criticality of the gapless spin sector in the initial Mott insulating ground state. However, after the pulse, we observed a saturation in correlation length and suppression of the spin correlations. At the same time, the entanglement entropy retains critical-like scaling $(S_{\chi} \sim a \log \chi)$ with a scaling coefficient a, raising the question about whether this reflects numerical artifacts from iMPS entanglement bounds or some kind of hidden criticality that could be verified through finite-size studies.

Besides that, several other directions for future research arise from this work. A detailed investigation of different pulse sequences and shapes such as multi-pulse protocols, time-asymmetric pulses, or gradual ramping might reveal stability and enhancement of photoinduced η -pairing beyond the single-pulse scenario. The robustness and dependence of the DQPT signature for different pulse parameters, shapes and sequences could also be explored. Furthermore, including more realistic features such as phonon coupling or multi-band effects would bring the simulations closer to experimental realizations. The cases of finite temperature and perturbed Hamiltonians have already been considered [14, 15].

In addition, the deviations from the predicted scaling coefficient κ for finite-entanglement scaling, as already mentioned, require further investigation.

In terms of methodology, other tensor network structures such as the multiscale entanglement renormalization ansatz (MERA) [117] could potentially provide a more accurate representation of the critical ground state. However, MERA is not commonly used for time evolution and the study of non-equilibrium dynamics, and its application to excited states remains exploratory.

In summary, while the iMPS ansatz has inherent limitations in representing highly entangled excited states with long-range order, it still captured essential physics of photoinduced phenomena and enabled insight into photoinduced η -pairing and DQPTs. This underscores the power and versatility of tensor network methods for simulating non-equilibrium quantum dynamics directly in the thermodynamic limit and points the way toward engineering novel quantum phenomena with light.

A. Additional Data

Tables A.1 to A.3 provide additional data on the deviations observed in the scaling coefficient κ discussed in Section 4.1.1. Specifically, they demonstrate both the dependence of these deviations on the bond dimension range as well as the consistency of the results for different models, methods, and parameters. The central charge, which was always computed with high accuracy, is also listed.

The increase in deviation with larger χ could suggest numerical convergence issues. However, as the data indicates, there is no significant difference between iTEBD and VUMPS, nor between different VUMPS convergence tolerances (Tab. A.3). This consistency suggests that numerical inaccuracies are unlikely to be the primary cause of the observed deviations.

To fully understand the origin of these deviations, a more detailed study would be required. Such an investigation would involve simulations at even larger bond dimensions, additional tests using iTEBD, and possibly iDMRG, as well as a systematic variation of algorithmic parameters. An analysis of the full entanglement spectrum would also be necessary to check the assumptions made in the derivation of the κ prediction [21]. Other assumptions such as the energy cost from discarding all but the largest χ eigenvalues could also be checked. Since this topic is not the main focus of the present work, a thorough investigation is left for future studies.

Half-filled Hubbard model, $U/t_h = 8$								
Method	χ_{\min} - χ_{\max}	κ	c	κ deviation				
VUMPS	25 - 100	1.314521	1.02283	2.1974 %				
VUMPS	25 - 500	1.301012	0.99672	3.2025~%				
VUMPS	25 - 1000	1.279962	0.99408	4.7687~%				
VUMPS	25 - 2500	1.263835	0.99426	5.9685~%				
VUMPS	100 - 2500	1.234573	0.99263	8.1457~%				
VUMPS	500 - 2500	1.220411	0.99814	9.1994~%				
VUMPS	750 - 2500	1.221147	0.99893	9.1446~%				
iTĒBD	50 - 1060	1.299046	1.0015	3.3488%				

Table A.1.: Finite-entanglement scaling results for the half-filled Hubbard model at $U/t_h=8$, using VUMPS and iTEBD over various bond dimension ranges. The exponent κ is extracted from the scaling $\xi_{\chi} \sim \chi^{\kappa}$, and the central charge c from $S \sim \frac{c}{6} \log \xi_{\chi}$. The final column shows the percentage deviation of κ from the theoretical prediction $\kappa_{\rm th}=1.344055$ (3.31). VUMPS was run with error tolerances $<10^{-8}$, and results are consistent across methods. The fits used to extract κ were linear regressions on log-log data, with Pearson correlation coefficients R>0.999 in all cases, indicating excellent agreement with power-law scaling.

Half-filled Hubbard model, $U/t_h = 0$								
Method	χ_{\min} - χ_{\max}	κ	c	κ deviation				
VUMPS	28 - 100	0.876782	1.99562	- 0.8150 %				
VUMPS	28 - 250	0.859904	2.00649	1.1257~%				
VUMPS	28 - 500	0.848623	2.01136	2.4228~%				
VUMPS	28 - 750	0.844952	2.00737	2.8449 %				
VUMPS	28 - 900	0.841547	2.00687	3.2364~%				
VUMPS	100 - 900	0.832892	1.98774	4.2316 %				
VUMPS	250 - 900	0.817954	1.99165	5.9492~%				

Table A.2.: Finite-entanglement scaling results for the half-filled Hubbard model at $U/t_h=0$, using VUMPS over various bond dimension ranges. The exponent κ and central charge c were extracted as in Tab. A.1. The percentage deviation from the theoretical prediction $\kappa_{\rm th}=0.869694$ (3.31) is shown in the last column. All fits yielded Pearson correlation coefficients R>0.998.

XX Model							
Method	VUMPS tolerance	$\chi_{ m min}$ - $\chi_{ m max}$	κ	c	κ deviation		
iTEBD	-	15 - 100	1.311252	0.99710	2.4406 %		
VUMPS	1e-12	16 - 100	1.318082	0.98897	1.9325%		
VUMPS	1e-11	16 - 100	1.320258	0.98872	1.7706 %		
VUMPS	1e-08	16 - 100	1.318355	0.99024	1.9122~%		
VUMPS	1e-06	16 - 100	1.319463	0.99194	1.8297~%		
VŪMPS	1e-12	16 - 200	1.298145	$0.99\overline{260}$	3.4158%		
VUMPS	1e-11	16 - 200	1.298481	0.99257	3.3908~%		
VUMPS	1e-08	16 - 200	1.298361	0.99324	3.3997~%		
VUMPS	1e-06	16 - 200	1.293965	0.99571	3.7268~%		
VUMPS	1e-11	16 - 300	1.286214	0.99363	4.3035%		
VUMPS	1e-08	16 - 300	1.286540	0.99403	4.2792~%		
VŪMPS	1e-11	60 - 300	1.263362	0.99306	-6.0037%		
VŪMPS	1e-11	100 - 300	1.242518	0.99885	$7.55\overline{46}\%$		

Table A.3.: Finite-entanglement scaling results for the critical XX model (c=1), using VUMPS and iTEBD. Results are shown for various VUMPS tolerances and bond dimension ranges. κ and c were extracted as in Tab. A.1, and compared to the theoretical prediction $\kappa_{\rm th} = 1.344055$ (3.31). Deviations persist even at strict tolerances, with all fits yielding R > 0.999.

- [1] A. Polkovnikov et al. "Colloquium: Nonequilibrium dynamics of closed interacting quantum systems". en. In: Reviews of Modern Physics 83.3 (Aug. 2011), pp. 863–883. DOI: 10.1103/RevModPhys.83.863.
- [2] J. Eisert, M. Friesdorf, and C. Gogolin. "Quantum many-body systems out of equilibrium". en. In: *Nature Physics* 11.2 (Feb. 2015), pp. 124–130. DOI: 10.1038/nphys3215.
- [3] I. Bloch, J. Dalibard, and W. Zwerger. "Many-body physics with ultracold gases". In: *Reviews of Modern Physics* 80.3 (July 2008), pp. 885–964. DOI: 10.1103/RevModPhys.80.885.
- [4] I. M. Georgescu, S. Ashhab, and F. Nori. "Quantum simulation". en. In: Reviews of Modern Physics 86.1 (Mar. 2014), pp. 153–185. DOI: 10.1103/RevModPhys.86.153.
- [5] R. Blatt and C. F. Roos. "Quantum simulations with trapped ions". en. In: *Nature Physics* 8.4 (Apr. 2012), pp. 277–284. DOI: 10.1038/nphys2252.
- I. Bloch, J. Dalibard, and S. Nascimbène. "Quantum simulations with ultracold quantum gases".
 en. In: Nature Physics 8.4 (Apr. 2012), pp. 267–276. DOI: 10.1038/nphys2259.
- [7] Roman Orus. "A Practical Introduction to Tensor Networks: Matrix Product States and Projected Entangled Pair States". en. In: *Annals of Physics* 349 (Oct. 2014), pp. 117–158. DOI: 10.1016/j.aop.2014.06.013.
- [8] Ulrich Schollwoeck. "The density-matrix renormalization group in the age of matrix product states". en. In: *Annals of Physics* 326.1 (Jan. 2011), pp. 96–192. DOI: 10.1016/j.aop.2010.09.012.
- [9] G. Vidal. "Classical Simulation of Infinite-Size Quantum Lattice Systems in One Spatial Dimension". In: *Phys. Rev. Lett.* 98.7 (Feb. 2007), p. 070201. DOI: 10.1103/PhysRevLett.98.070201.
- [10] Laurens Vanderstraeten, Jutho Haegeman, and Frank Verstraete. "Tangent-space methods for uniform matrix product states". en. In: SciPost Physics Lecture Notes (Jan. 2019), p. 7. DOI: 10.21468/SciPostPhysLectNotes.7.
- [11] V. Zauner-Stauber et al. "Variational optimization algorithms for uniform matrix product states". In: *Phys. Rev. B* 97.4 (Jan. 2018), p. 045145. DOI: 10.1103/PhysRevB.97.045145.
- [12] F. H. L. Essler et al. *The One-Dimensional Hubbard Model*. Cambridge: Cambridge University Press, 2005. DOI: 10.1017/CB09780511534843.
- [13] Chen Ning Yang. "η pairing and off-diagonal long-range order in a Hubbard model". en. In: Physical Review Letters 63.19 (Nov. 1989), pp. 2144–2147. DOI: 10.1103/PhysRevLett.63. 2144.
- [14] Tatsuya Kaneko et al. "Photoinduced η Pairing in the Hubbard Model". en. In: *Physical Review Letters* 122.7 (Feb. 2019), p. 077002. DOI: 10.1103/PhysRevLett.122.077002.
- [15] S. Ejima et al. "Photoinduced η -pairing at finite temperatures". en. In: *Physical Review Research* 2.3 (July 2020), p. 032008. DOI: 10.1103/PhysRevResearch.2.032008.
- [16] S. Ejima et al. "Photoinduced η -pairing in One-dimensional Mott Insulators". en. In: Proceedings of the International Conference on Strongly Correlated Electron Systems (SCES2019). Okayama, Japan: Journal of the Physical Society of Japan, Mar. 2020. DOI: 10.7566/JPSCP.30.011184.

- [17] C. N. Yang. "Concept of Off-Diagonal Long-Range Order and the Quantum Phases of Liquid He and of Superconductors". en. In: *Reviews of Modern Physics* 34.4 (Oct. 1962), pp. 694–704. DOI: 10.1103/RevModPhys.34.694.
- [18] M. Heyl. "Dynamical quantum phase transitions: a review". en. In: Reports on Progress in Physics 81.5 (May 2018), p. 054001. DOI: 10.1088/1361-6633/aaaf9a.
- [19] M. Heyl, A. Polkovnikov, and S. Kehrein. "Dynamical Quantum Phase Transitions in the Transverse-Field Ising Model". en. In: *Physical Review Letters* 110.13 (Mar. 2013), p. 135704. DOI: 10.1103/PhysRevLett.110.135704.
- [20] L. Tagliacozzo et al. "Scaling of entanglement support for Matrix Product States". In: *Physical Review B* 78 (Jan. 2008). DOI: 10.1103/PhysRevB.78.024410.
- [21] F. Pollmann et al. "Theory of Finite-Entanglement Scaling at One-Dimensional Quantum Critical Points". en. In: *Physical Review Letters* 102.25 (June 2009), p. 255701. DOI: 10.1103/PhysRevLett.102.255701.
- [22] C. Cohen-Tannoudji, B. Diu, and F. Laloë. *Quantenmechanik: Band 2.* de. De Gruyter, July 2019. DOI: 10.1515/9783110638769.
- [23] C. Cohen-Tannoudji, B. Diu, and F. Laloë. Quantenmechanik Band 3: Fermionen, Bosonen, Photonen, Korrelationen und Verschränkung. de. De Gruyter, Aug. 2020. DOI: 10.1515/9783110649130.
- [24] G. Czycholl. *Theoretische Festkörperphysik Band 1.* de. Berlin, Heidelberg: Springer, 2016. DOI: 10.1007/978-3-662-47141-8.
- [25] C. Kim et al. "Separation of spin and charge excitations in one-dimensional SrCuO2". In: *Physical Review B* 56.24 (Dec. 1997), pp. 15589–15595. DOI: 10.1103/PhysRevB.56.15589.
- [26] R. Neudert et al. "Manifestation of Spin-Charge Separation in the Dynamic Dielectric Response of One-Dimensional Sr2CuO3". en. In: *Physical Review Letters* 81.3 (July 1998), pp. 657–660. DOI: 10.1103/PhysRevLett.81.657.
- [27] S. M. Griffin et al. "A bespoke single-band Hubbard model material". en. In: *Physical Review B* 93.7 (Feb. 2016), p. 075115. DOI: 10.1103/PhysRevB.93.075115.
- [28] H.-P. Eckle. Models of Quantum Matter: A First Course on Integrability and the Bethe Ansatz. en. 1st ed. Oxford University PressOxford, July 2019. DOI: 10.1093/oso/9780199678839.001. 0001.
- [29] J. González, ed. Quantum electron liquids and high-Tc superconductivity. en. Lecture notes in physics m38. Berlin; New York: Springer, 1995.
- [30] Thierry Giamarchi. Quantum physics in one dimension. eng. The international series of monographs on physics 121. Oxford Oxford New York: Clarendon Press Oxford university press, 2004.
- [31] H. J. Schulz. Fermi liquids and non-Fermi liquids. Mar. 1995. DOI: 10.48550/arXiv.cond-mat/9503150.
- [32] S. Ejima and S. Nishimoto. "Phase Diagram of the One-Dimensional Half-Filled Extended Hubbard Model". en. In: *Physical Review Letters* 99.21 (Nov. 2007), p. 216403. DOI: 10.1103/PhysRevLett.99.216403.
- [33] Gerd Czycholl. Theoretische Festkörperphysik Band 2: Anwendungen: Nichtgleichgewicht, Verhalten in äußeren Feldern, kollektive Phänomene. de. Berlin, Heidelberg: Springer Berlin Heidelberg, 2017. DOI: 10.1007/978-3-662-53701-5.

[34] F. Woynarovich and H. .-. Eckle. "Finite-size corrections for the low lying states of a half-filled Hubbard chain". en. In: *Journal of Physics A: Mathematical and General* 20.7 (May 1987), pp. L443–L449. DOI: 10.1088/0305-4470/20/7/005.

- [35] Jan De Boer, Vladimir E. Korepin, and Andreas Schadschneider. "η Pairing as a Mechanism of Superconductivity in Models of Strongly Correlated Electrons". en. In: *Physical Review Letters* 74.5 (Jan. 1995), pp. 789–792. DOI: 10.1103/PhysRevLett.74.789.
- [36] F. H. L. Essler, V. E. Korepin, and K. Schoutens. "New exactly solvable model of strongly correlated electrons motivated by high- T c superconductivity". en. In: *Physical Review Letters* 68.19 (May 1992), pp. 2960–2963. DOI: 10.1103/PhysRevLett.68.2960.
- [37] G. L. Sewell. "Off-diagonal long-range order and the Meissner effect". en. In: Journal of Statistical Physics 61.1-2 (Oct. 1990), pp. 415–422. DOI: 10.1007/BF01013973.
- [38] H. T. Nieh, G. Su, and B.-H. Zhao. "Off-diagonal long-range order: Meissner effect and flux quantization". In: *Physical Review B* 51.6 (Feb. 1995), pp. 3760–3764. DOI: 10.1103/PhysRevB. 51.3760.
- [39] L. Amico et al. "Entanglement in many-body systems". en. In: Reviews of Modern Physics 80.2 (May 2008), pp. 517–576. DOI: 10.1103/RevModPhys.80.517.
- [40] Michael A. Nielsen and Isaac L. Chuang. *Quantum computation and quantum information*. eng. 10th anniversary edition. Cambridge: Cambridge university press, 2010.
- [41] S. Ishihara. "Photoinduced Ultrafast Phenomena in Correlated Electron Magnets". In: *Journal of the Physical Society of Japan* 88.7 (July 2019), p. 072001. DOI: 10.7566/JPSJ.88.072001.
- [42] K. Yonemitsu and K. Nasu. "Theory of photoinduced phase transitions in itinerant electron systems". en. In: *Physics Reports* 465.1 (Aug. 2008), pp. 1–60. DOI: 10.1016/j.physrep.2008.04.008.
- [43] D. N. Basov, R. D. Averitt, and D. Hsieh. "Towards properties on demand in quantum materials". en. In: *Nature Materials* 16.11 (Nov. 2017), pp. 1077–1088. DOI: 10.1038/nmat5017.
- [44] H. Ichikawa et al. "Transient photoinduced 'hidden' phase in a manganite". en. In: *Nature Materials* 10.2 (Feb. 2011), pp. 101–105. DOI: 10.1038/nmat2929.
- [45] S. Mor et al. "Ultrafast Electronic Band Gap Control in an Excitonic Insulator". In: *Physical Review Letters* 119.8 (Aug. 2017), p. 086401. DOI: 10.1103/PhysRevLett.119.086401.
- [46] M. Mitrano et al. "Possible light-induced superconductivity in K3C60 at high temperature". en. In: *Nature* 530.7591 (Feb. 2016), pp. 461–464. DOI: 10.1038/nature16522.
- [47] S. Kaiser et al. "Optically induced coherent transport far above Tc in underdoped YBa2Cu3O6+ δ ". en. In: *Physical Review B* 89.18 (May 2014), p. 184516. DOI: 10.1103/PhysRevB.89.184516.
- [48] W. Hu et al. "Optically enhanced coherent transport in YBa2Cu3O6.5 by ultrafast redistribution of interlayer coupling". en. In: *Nature Materials* 13.7 (July 2014), pp. 705–711. DOI: 10.1038/nmat3963.
- [49] D. Fausti et al. "Light-Induced Superconductivity in a Stripe-Ordered Cuprate". en. In: Science 331.6014 (Jan. 2011), pp. 189–191. DOI: 10.1126/science.1197294.
- [50] G. Mazza and A. Georges. "Nonequilibrium superconductivity in driven alkali-doped fullerides". en. In: *Physical Review B* 96.6 (Aug. 2017), p. 064515. DOI: 10.1103/PhysRevB.96.064515.
- [51] K. Ido, T. Ohgoe, and M. Imada. "Correlation-induced superconductivity dynamically stabilized and enhanced by laser irradiation". en. In: Science Advances 3.8 (Aug. 2017), e1700718. DOI: 10.1126/sciadv.1700718.

- [52] M. A. Sentef et al. "Theory of light-enhanced phonon-mediated superconductivity". en. In: *Physical Review B* 93.14 (Apr. 2016), p. 144506. DOI: 10.1103/PhysRevB.93.144506.
- [53] D. M. Kennes et al. "Transient superconductivity from electronic squeezing of optically pumped phonons". en. In: *Nature Physics* 13.5 (May 2017), pp. 479–483. DOI: 10.1038/nphys4024.
- [54] J. Tindall et al. "Heating-Induced Long-Range η Pairing in the Hubbard Model". en. In: *Physical Review Letters* 123.3 (July 2019), p. 030603. DOI: 10.1103/PhysRevLett.123.030603.
- [55] F. Peronaci, O. Parcollet, and M. Schiró. "Enhancement of local pairing correlations in periodically driven Mott insulators". en. In: *Physical Review B* 101.16 (Apr. 2020), p. 161101. DOI: 10.1103/PhysRevB.101.161101.
- [56] J. Li et al. "η-paired superconducting hidden phase in photodoped Mott insulators". en. In: *Physical Review B* 102.16 (Oct. 2020), p. 165136. DOI: 10.1103/PhysRevB.102.165136.
- [57] R. Fujiuchi et al. "Photoinduced electron-electron pairing in the extended Falicov-Kimball model". en. In: *Physical Review B* 100.4 (July 2019), p. 045121. DOI: 10.1103/PhysRevB. 100.045121.
- [58] R. Fujiuchi et al. "Superconductivity and charge density wave under a time-dependent periodic field in the one-dimensional attractive Hubbard model". en. In: *Physical Review B* 101.23 (June 2020), p. 235122. DOI: 10.1103/PhysRevB.101.235122.
- [59] S. Kitamura and H. Aoki. "η -pairing superfluid in periodically-driven fermionic Hubbard model with strong attraction". en. In: *Physical Review B* 94.17 (Nov. 2016), p. 174503. DOI: 10.1103/ PhysRevB.94.174503.
- [60] T. Kaneko, S. Yunoki, and A. J. Millis. "Charge stiffness and long-range correlation in the optically induced η-pairing state of the one-dimensional Hubbard model". en. In: Physical Review Research 2.3 (July 2020), p. 032027. DOI: 10.1103/PhysRevResearch.2.032027.
- [61] R. Peierls. "Zur Theorie des Diamagnetismus von Leitungselektronen". de. In: Zeitschrift für Physik 80.11 (Nov. 1933), pp. 763–791. DOI: 10.1007/BF01342591.
- [62] U. Divakaran, S. Sharma, and A. Dutta. "Tuning the presence of dynamical phase transitions in a generalized XY spin chain". en. In: *Physical Review E* 93.5 (May 2016), p. 052133. DOI: 10.1103/PhysRevE.93.052133.
- [63] T. Puskarov and D. Schuricht. "Time evolution during and after finite-time quantum quenches in the transverse-field Ising chain". en. In: SciPost Physics 1.1 (Oct. 2016), p. 003. DOI: 10. 21468/SciPostPhys.1.1.003.
- [64] S. Sharma et al. "Slow quenches in a quantum Ising chain: Dynamical phase transitions and topology". en. In: *Physical Review B* 93.14 (Apr. 2016), p. 144306. DOI: 10.1103/PhysRevB. 93.144306.
- [65] S. Sharma, S. Suzuki, and A. Dutta. "Quenches and dynamical phase transitions in a nonintegrable quantum Ising model". en. In: *Physical Review B* 92.10 (Sept. 2015), p. 104306. DOI: 10.1103/PhysRevB.92.104306.
- [66] U. Bhattacharya and A. Dutta. "Interconnections between equilibrium topology and dynamical quantum phase transitions in a linearly ramped Haldane model". en. In: *Physical Review B* 95.18 (May 2017), p. 184307. DOI: 10.1103/PhysRevB.95.184307.
- [67] M. Azimi et al. "Pulse and quench induced dynamical phase transition in a chiral multiferroic spin chain". en. In: *Physical Review B* 94.6 (Aug. 2016), p. 064423. DOI: 10.1103/PhysRevB. 94.064423.
- [68] K. Yang et al. "Floquet dynamical quantum phase transitions". en. In: *Physical Review B* 100.8 (Aug. 2019), p. 085308. DOI: 10.1103/PhysRevB.100.085308.

[69] J. Naji et al. "Engineering Floquet dynamical quantum phase transitions". en. In: *Physical Review B* 106.9 (Sept. 2022), p. 094314. DOI: 10.1103/PhysRevB.106.094314.

- [70] F. Pollmann et al. "Dynamics after a sweep through a quantum critical point". en. In: *Physical Review E* 81.2 (Feb. 2010), p. 020101. DOI: 10.1103/PhysRevE.81.020101.
- [71] A. LeClair et al. "Boundary energy and boundary states in integrable quantum field theories". en. In: Nuclear Physics B 453.3 (Oct. 1995), pp. 581–618. DOI: 10.1016/0550-3213(95)00435-U.
- [72] M. E. Fishert. "THE NATURE OF CRITICAL POINTS". en. In: (1965).
- [73] P. Pfeuty. "The one-dimensional Ising model with a transverse field". In: Annals of Physics 57.1 (Mar. 1970), pp. 79–90. DOI: 10.1016/0003-4916(70)90270-8.
- [74] M. Heyl. "Scaling and Universality at Dynamical Quantum Phase Transitions". en. In: *Physical Review Letters* 115.14 (Oct. 2015), p. 140602. DOI: 10.1103/PhysRevLett.115.140602.
- [75] J. C. Budich and M. Heyl. "Dynamical topological order parameters far from equilibrium". en. In: *Physical Review B* 93.8 (Feb. 2016), p. 085416. DOI: 10.1103/PhysRevB.93.085416.
- [76] J. Zhang et al. "Observation of a many-body dynamical phase transition with a 53-qubit quantum simulator". en. In: *Nature* 551.7682 (Nov. 2017), pp. 601–604. DOI: 10.1038/nature24654.
- [77] P. Jurcevic et al. "Direct Observation of Dynamical Quantum Phase Transitions in an Interacting Many-Body System". en. In: *Physical Review Letters* 119.8 (Aug. 2017), p. 080501. DOI: 10.1103/PhysRevLett.119.080501.
- [78] N. Fläschner et al. "Observation of a dynamical topological phase transition". In: *Nature Physics* 14.3 (Mar. 2018), pp. 265–268. DOI: 10.1038/s41567-017-0013-8.
- [79] X.-Y. Guo et al. "Observation of a Dynamical Quantum Phase Transition by a Superconducting Qubit Simulation". en. In: *Physical Review Applied* 11.4 (Apr. 2019), p. 044080. DOI: 10.1103/PhysRevApplied.11.044080.
- [80] K. Wang et al. "Simulating Dynamic Quantum Phase Transitions in Photonic Quantum Walks". en. In: Physical Review Letters 122.2 (Jan. 2019), p. 020501. DOI: 10.1103/PhysRevLett.122.020501.
- [81] X. Nie et al. "Experimental Observation of Equilibrium and Dynamical Quantum Phase Transitions via Out-of-Time-Ordered Correlators". en. In: *Physical Review Letters* 124.25 (June 2020), p. 250601. DOI: 10.1103/PhysRevLett.124.250601.
- [82] J. C. Bridgeman and C. T. Chubb. *Hand-waving and Interpretive Dance: An Introductory Course on Tensor Networks*. May 2017. DOI: 10.48550/arXiv.1603.03039.
- [83] J. Eisert. "Entanglement and tensor network states". In: Autumn School on Correlated Electrons: Emergent Phenomena in Correlated Matter, Juelich. Ed. by E. Pavarini, E. Koch, and U. Schollwöck. 2013. URL: https://arxiv.org/abs/1308.3318.
- [84] D. Perez-Garcia et al. *Matrix Product State Representations*. en. May 2007. URL: http://arxiv.org/abs/quant-ph/0608197.
- [85] Tao Xiang. Density Matrix and Tensor Network Renormalization. en. 1st ed. Cambridge University Press, Aug. 2023. DOI: 10.1017/9781009398671.
- [86] Jan von Delft. Lecture Tensor Networks 2022 Fakultät für Physik LMU München. de. 2022. URL: https://www2.physik.uni-muenchen.de/lehre/vorlesungen/sose_22/tensor_networks_22/index.html.
- [87] J. Eisert, M. Cramer, and M. B. Plenio. "Colloquium: Area laws for the entanglement entropy". In: Rev. Mod. Phys. 82.1 (Feb. 2010), pp. 277–306. DOI: 10.1103/RevModPhys.82.277.

- [88] Pasquale Calabrese and John Cardy. "Entanglement Entropy and Quantum Field Theory". en. In: Journal of Statistical Mechanics: Theory and Experiment 2004.06 (June 2004), P06002. DOI: 10.1088/1742-5468/2004/06/P06002.
- [89] B. Swingle and J. McGreevy. "Area law for gapless states from local entanglement thermodynamics". en. In: *Physical Review B* 93.20 (May 2016), p. 205120. DOI: 10.1103/PhysRevB.93. 205120.
- [90] M. B. Hastings. "An area law for one-dimensional quantum systems". In: J. Stat. Mech. P08024 (2007). URL: https://doi.org/10.1088/1742-5468/2007/08/P08024.
- [91] E. Bianchi et al. Volume-law entanglement entropy of typical pure quantum states. July 2022. DOI: 10.1103/PRXQuantum.3.030201.
- [92] H.-H. Lai and K. Yang. "Entanglement entropy scaling laws and eigenstate typicality in free fermion systems". en. In: *Physical Review B* 91.8 (Feb. 2015), p. 081110. DOI: 10.1103/PhysRevB.91.081110.
- [93] V. Zauner-Stauber and J. C. Halimeh. "Probing the anomalous dynamical phase in long-range quantum spin chains through Fisher-zero lines". en. In: *Physical Review E* 96.6 (Dec. 2017), p. 062118. DOI: 10.1103/PhysRevE.96.062118.
- [94] C. Karrasch and D. Schuricht. "Dynamical phase transitions after quenches in nonintegrable models". en. In: *Physical Review B* 87.19 (May 2013), p. 195104. DOI: 10.1103/PhysRevB.87.195104.
- [95] ITensor/ITensorInfiniteMPS.jl. May 2025. URL: https://github.com/ITensor/ITensorInfiniteMPS.jl.
- [96] Matthew Fishman, Steven White, and Edwin Stoudenmire. "The ITensor Software Library for Tensor Network Calculations". en. In: *SciPost Physics Codebases* (Aug. 2022), p. 4. DOI: 10.21468/SciPostPhysCodeb.4.
- [97] ITensor. URL: http://itensor.org/.
- [98] M. Fishman, S. R. White, and E. M. Stoudenmire. "Codebase release 0.3 for ITensor". In: SciPost Phys. Codebases (2022), 4–r0.3. DOI: 10.21468/SciPostPhysCodeb.4-r0.3.
- [99] G. Vidal. "Efficient Classical Simulation of Slightly Entangled Quantum Computations". In: *Physical Review Letters* 91.14 (Oct. 2003), p. 147902. DOI: 10.1103/PhysRevLett.91.147902.
- [100] G. Vidal. "Efficient Simulation of One-Dimensional Quantum Many-Body Systems". In: *Physical Review Letters* 93.4 (July 2004), p. 040502. DOI: 10.1103/PhysRevLett.93.040502.
- [101] Masuo Suzuki. "Fractal decomposition of exponential operators with applications to many-body theories and Monte Carlo simulations". en. In: *Physics Letters A* 146.6 (June 1990), pp. 319–323. DOI: 10.1016/0375-9601(90)90962-N.
- [102] R. Orús and G. Vidal. "Infinite time-evolving block decimation algorithm beyond unitary evolution". In: *Phys. Rev. B* 78.15 (Oct. 2008), p. 155117. DOI: 10.1103/PhysRevB.78.155117.
- [103] M. B. Hastings. Light Cone Matrix Product. Mar. 2009. URL: http://arxiv.org/abs/0903. 3253.
- [104] ITensor: Fermions and Jordan-Wigner String. URL: https://itensor.org/docs.cgi?page=tutorials/fermions.
- [105] J. Voit. "One-Dimensional Fermi liquids". In: Reports on Progress in Physics 58.9 (Sept. 1995), pp. 977–1116. DOI: 10.1088/0034-4885/58/9/002.

[106] P. Chen et al. "Entanglement entropy scaling of the XXZ chain". In: Journal of Statistical Mechanics: Theory and Experiment 2013.10 (Oct. 2013), P10007. DOI: 10.1088/1742-5468/ 2013/10/P10007.

- [107] S. Ejima, F. Lange, and H. Fehske. "Entanglement analysis of photoinduced \$\$\eta\$\$-pairing states". en. In: *The European Physical Journal Special Topics* 232.20-22 (Dec. 2023), pp. 3479–3482. DOI: 10.1140/epjs/s11734-023-00975-6.
- [108] P. Calabrese and J. Cardy. "Quantum quenches in 1 + 1 dimensional conformal field theories". en. In: *Journal of Statistical Mechanics: Theory and Experiment* 2016.6 (June 2016), p. 064003. DOI: 10.1088/1742-5468/2016/06/064003.
- [109] P. Calabrese and J. Cardy. "Quantum quenches in extended systems". en. In: Journal of Statistical Mechanics: Theory and Experiment 2007.06 (June 2007), P06008–P06008. DOI: 10.1088/1742-5468/2007/06/P06008.
- [110] P. Calabrese and J. Cardy. "Time Dependence of Correlation Functions Following a Quantum Quench". en. In: *Physical Review Letters* 96.13 (Apr. 2006), p. 136801. DOI: 10.1103/PhysRevLett.96.136801.
- [111] M. Frasca. Strong Coupling Perturbation Theory in Quantum Mechanics. July 2003. DOI: 10. 48550/arXiv.quant-ph/0307237.
- [112] Juan José Mendoza-Arenas. "Dynamical quantum phase transitions in the one-dimensional extended Fermi-Hubbard model". In: *Journal of Statistical Mechanics: Theory and Experiment* 2022.4 (Apr. 2022), p. 043101. DOI: 10.1088/1742-5468/ac6031.
- [113] P. Calabrese and J. Cardy. "Evolution of Entanglement Entropy in One-Dimensional Systems". en. In: *Journal of Statistical Mechanics: Theory and Experiment* 2005.04 (Apr. 2005), P04010. DOI: 10.1088/1742-5468/2005/04/P04010.
- [114] V. Alba and P. Calabrese. "Entanglement and thermodynamics after a quantum quench in integrable systems". en. In: *Proceedings of the National Academy of Sciences* 114.30 (July 2017), pp. 7947–7951. DOI: 10.1073/pnas.1703516114.
- [115] M. A. Cazalilla and M.-C. Chung. "Quantum quenches in the Luttinger model and its close relatives". en. In: Journal of Statistical Mechanics: Theory and Experiment 2016.6 (June 2016), p. 064004. DOI: 10.1088/1742-5468/2016/06/064004.
- [116] S. Paul, P. Titum, and M. Maghrebi. "Hidden quantum criticality and entanglement in quench dynamics". en. In: *Physical Review Research* 6.3 (July 2024), p. L032003. DOI: 10.1103/PhysRevResearch.6.L032003.
- [117] G. Vidal. "Class of Quantum Many-Body States That Can Be Efficiently Simulated". en. In: Physical Review Letters 101.11 (Sept. 2008), p. 110501. DOI: 10.1103/PhysRevLett.101.110501.

Acknowledgements

I would like to thank PD Dr. Satoshi Ejima for proposing the topic, supervising this thesis, and for always being available to answer my questions.

I also want to thank everyone at DLR for providing a positive working environment.

I thank Prof. Dr. Dieter Jaksch for readily agreeing to be the second examiner of my thesis.

Special thanks go to my family for their continuous support.

Finally, a very special thanks goes to Balu for being there for me for half my life, and practically until the completion of this thesis. You will continue to be with me in spirit.

Eidesstattliche Erklärung

Hiermit versichere ich an Eides statt, dass ich die vorliegende Arbeit im Bachelorstudiengang Computing in Science selbstständig verfasst und keine anderen als die angegebenen Hilfsmittel – insbesondere keine im Quellenverzeichnis nicht benannten Internet-Quellen – benutzt habe. Alle Stellen, die wörtlich oder sinngemäß aus Veröffentlichungen entnommen wurden, sind als solche kenntlich gemacht. Ich versichere weiterhin, dass ich die Arbeit vorher nicht in einem anderen Prüfungsverfahren eingereicht habe. Sofern im Zuge der Erstellung der vorliegenden Abschlussarbeit generative Künstliche Intelligenz (gKI) basierte elektronische Hilfsmittel verwendet wurden, versichere ich, dass meine eigene Leistung im Vordergrund stand und dass eine vollständige Dokumentation aller verwendeten Hilfsmittel gemäß der Guten Wissenschaftlichen Praxis vorliegt. Ich trage die Verantwortung für eventuell durch die gKI generierte fehlerhafte oder verzerrte Inhalte, fehlerhafte Referenzen, Verstöße gegen das Datenschutzund Urheberrecht oder Plagiate.

Hamburg, den 24.06.2025

Pascal Sievers

Vorname Nachname